Fatigue Crack Growth Fundamentals in Shape Memory Alloys

Y. Wu[1] · A. Ojha[1] · L. Patriarca[1] · H. Sehitoglu[1]

Published online: 22 April 2015

Introduction

The shape memory alloys used in engineering and biomedical applications undergo repeated (cyclic) deformation [1, 2]. These alloys undergo reversible, thermo-elastic phase transformations at the macro-scale, while a degree of irreversibility exists when slip occurs locally at micro-scale. The fatigue damage tolerance of these alloys has been a tremendous concern, yet an understanding remains elusive as of today. This is partly because our knowledge of fatigue crack growth is built upon *untransforming* alloys, while the *transformation* behavior modifies the driving force parameters. In the case of *untransforming* materials, the stress intensity factor and the crack tip displacements are used to characterize fatigue crack growth. In the case of shape memory alloys, these parameters change but the exact nature of the changes in the driving force that occur has not been derived.

Table 1 illustrates the mechanisms that have been forwarded to modify the driving forces in the presence of phase transformation from austenite to martensite. The modifications in driving force due to internal tractions (first row) have been derived by Rice–McMeeking–Evans [3, 4] using weight function theory. The transformation strains drive these tractions. Also as shown in Table 1 (second row), there have been several efforts attempting to calculate the redistribution of stress fields ahead of the crack tip due to the phase transformation. These analyses [5], similar to the work of Irwin on plastic zone size correction [6], propose a change in effective crack length, resulting in a change in the stress intensity factor. A number of recent works on the numerical [7–9] determination of transformation zones under monotonic deformation have been undertaken. The local driving forces are found to differ compared to remotely evaluated levels.

✉ H. Sehitoglu
huseyin@illinois.edu

[1] Department of Mechanical Science and Engineering, University of Illinois at Urbana-Champaign, Urbana, IL 61801, USA

There have been previous fundamental works on fatigue crack initiation in shape memory alloys [10–16] describing the role of slip, the origin of irreversibilities, and residual martensite, but much less work has been undertaken on fatigue crack growth behavior. Systematic efforts have been undertaken by Ritchie and his students [17–19] on experimental fatigue crack growth studies on NiTi alloys. Overall, the measured threshold stress intensity levels were rather low (less than 3 MPa$\sqrt{\text{m}}$) in NiTi. Other papers confirmed the low fatigue crack growth resistance of shape memory alloys in general [13, 20, 21]; however, the calculation of effective stress intensity in fatigue remains unresolved.

We note that under cycling loading eigenstrains (misfit strains) arise when transformation develops in the matrix. Under fatigue conditions both the maximum stress intensity and minimum stress intensity levels are modified due to the transformation effects. The maximum stress intensity (Fig. 1a) is reduced as $K_{\text{red}-\max}$ while the minimum stress intensity is decreased by $K_{\text{red}-\min}$ resulting in a net reduction of the stress intensity range, rendering an effective range denoted as $\Delta K_{\text{eff}} = \Delta K - \Delta K_{\text{red}}$ (shaded region). In this work, we propose a cal-culation methodology for these quantities. The effective stress intensity range would remain the same if the reductions of stress intensity at maximum and minimum loads were identical.

Because we are considering the differential reduction in maximum and minimum stress intensity, the consideration of moduli difference between martensite and austenite domains becomes significant. The martensite under consideration is 'oriented martensite' and not the 'thermally induced martensite' [22]. The elastic moduli of oriented martensite differ from the thermally induced one and also from the austenite moduli, and this difference cannot be ignored. The martensite crystal moduli tensor (monoclinic or tetragonal depending on the alloys considered here) has higher number of independent constants than the cubic austenite. Also, in this study, our experiments utilize single crystals of austenite permitting precise knowledge of the elastic constants.

In Fig. 1b, the main variables that influence the transformation mediated fatigue crack growth rate are listed. The equivalent eigenstrain, e^{**}_{mn}, is calculated from Eshelby's equivalent inclusion principle; the crack length, a; transformation height in the crack wake, w; the elastic moduli of the austenite, C_{ijkl}; and martensite, C'_{ijkl}, phases respectively (see Fig. 1b). Because the stress state at the crack tip is rather complex, the resulting strain distribution is difficult to predict but it can be measured experimentally. Even though the residual strain per one cycle is very small, it accumulates over many fatigue cycles. The crack length and transformation zone height in the wake can also be obtained through experiments. The elastic moduli can also be measured for the austenite single crystals, while density

Table 1 A summary of the mechanisms at crack tips undergoing transformation under loading

Type of loading-mechanism	Schematic	Important variables	References
Monotonic loading-shielding associated with tractions	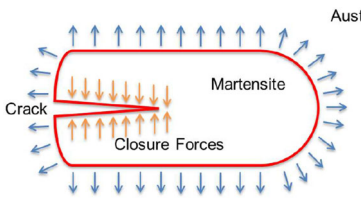	Dimensions of the residual transformation zone in the crack wake, tractions cancel ahead of tip but substantial on crack faces	[3, 4]
Monotonic loading-modification of crack tip stress fields	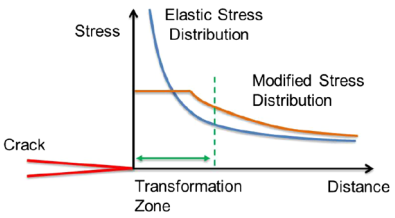	Redistribution of stress fields ahead of crack tip, stress state dependence of transformation zone	[5]
Fatigue loading-closure force differential at max. and min. loads	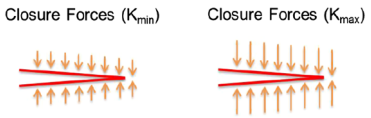	Elastic moduli (crystallography), transformation zone (verified with DIC), residual transformation strain, reduction of stress intensity range	This study

The tractions due to transformation are shown at the austenite to martensite interface. The differences of closure forces at the minimum and maximum stress intensity levels are important in fatigue case (this study)

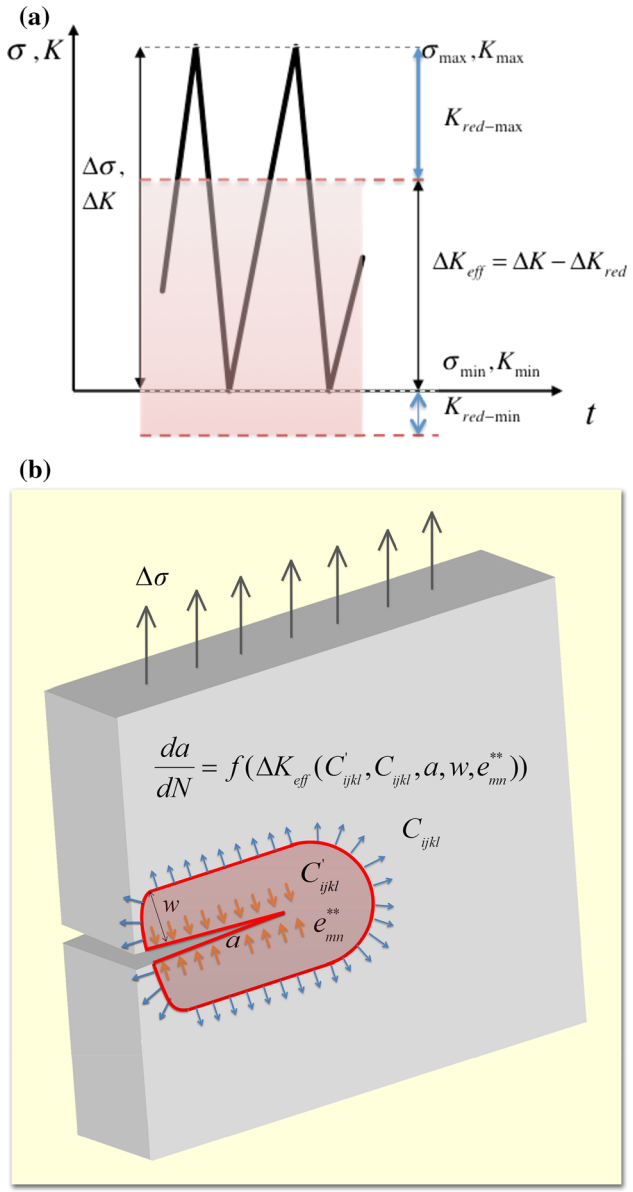

Fig. 1 **a** The full stress intensity range, the reductions in maximum and minimum stress intensity levels due to transformation induced tractions. The definition of an effective stress intensity range is shown. Note that $\Delta K_{\text{eff}} = \Delta K - \Delta K_{\text{red}} = \Delta K - (K_{\text{red-max}} - K_{\text{red-min}})$. **b** Schematic of fatigue crack growing in a shape memory material. The effective stress intensity range is influenced by the residual transformation zone (*colored red*), the equivalent eigenstrain dictated by the moduli tensors of austenite and martensite, and the internal tractions indicated with *arrows*. Note that eigenstrain corresponding to maximum and minimum loads are calculated

function theory (DFT) calculations need to be utilized in the case of martensite. Considering all the factors, we postulate that the fatigue crack growth rate is given as a function of C'_{ijkl}, C_{ijkl}, a, w, and e^{**}_{mn}, as $\frac{da}{dN} = f(\Delta K_{\text{eff}}(C'_{ijkl}, C_{ijkl}, a, w, e^{**}_{mn}))$. Experimentally, crack tip displacements field measurements can be used to extract stress intensity levels. In the first approach (Method I) of the current work, the displacement fields are measured in the vicinity of crack tip during fatigue experiments with digital image correlation (DIC). These displacement results can be utilized in turn to determine the 'effective stress intensity' levels. In the case of transforming alloys, these measured displacement fields would naturally reflect the crack tip driving force modification in the presence of transformation strains. As an extension of the method using regression, it is worthwhile to measure the contact of crack surfaces during fatigue resulting in crack closure. Such experiments are now possible with the use of virtual extensometers behind the crack tip in conjunction with digital image correlation studies. We explore this possibility as well in the current work accounting for a full range of mechanisms. The results from regression and virtual extensometers agreed in untransforming alloys, and a similar agreement is expected in shape memory materials. Alternately, in the second approach (Method II), we compute the modified stress intensity in transforming alloys due to internal tractions. In fatigue loading, one needs to consider tractions at both maximum and minimum loads imposed on the transforming regions by the surrounding untransformed domains. Ideally, both approaches (I and II) should render an 'effective stress intensity range' that is comparable in magnitude resulting in the true value of the driving force in fatigue.

To develop an appreciation of the length scales for the experimental and modeling work pursued in this work, we include Fig. 2. At the smallest length scales, atomistic simulations provide a critical resource to establish the elastic constants [22–24] of austenite and martensite which can be substantially different. At the higher length scale, a micro-mechanics analysis is undertaken to determine the closure forces in the wake of the crack tip. Consideration of the theoretical transformation strains and experimentally measured transformation strains are taken into account. The modeling results are verified by precise measurements of crack tip displacements with DIC, and closure stress levels are determined with virtual extensometers at the macro-scale. The paper will cover the entire length scales in Fig. 2 with theory and experimentation.

In summary, the driving force for fatigue crack growth in shape memory alloys (the effective stress intensity range) requires additional calculations and depends on the closure forces at both maximum and minimum load, the elastic moduli of austenite and martensite and their anisotropy. The irreversible (residual) strain accumulates with cycles and the residual transformation strain in the crack wake produces closure forces. In turn, such forces contribute significantly to setting an 'effective stress intensity range' lower than the theoretical one. In the present work utilizing anisotropic elasticity theory, Eshelby's equivalent inclusion principle [25], weight function

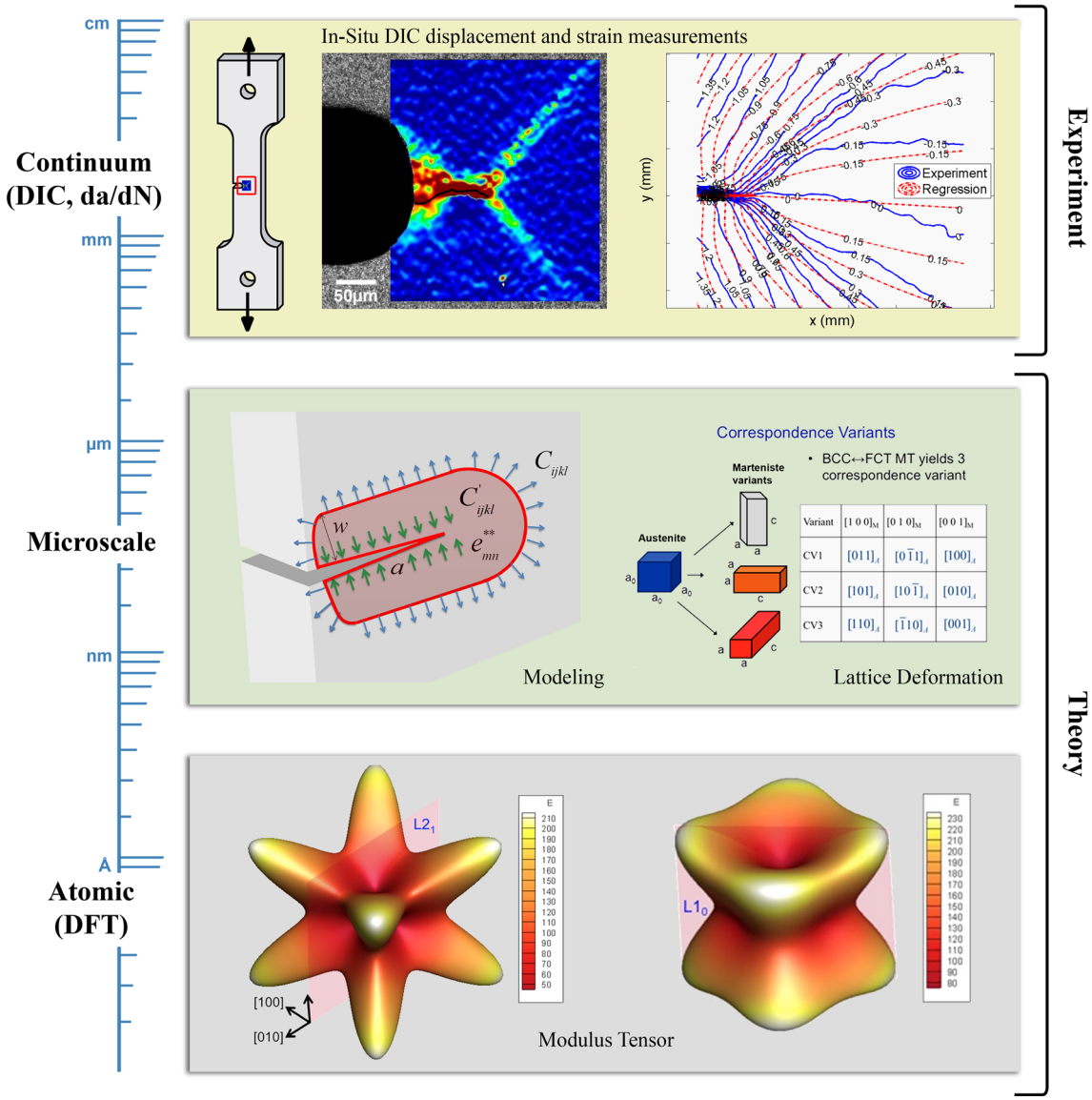

Fig. 2 The methodology utilized in the present work. At the atomic scale, the elastic moduli tensor is determined through ab initio calculations, at the micro scale quantities such as transformation strain and the modification of crack driving forces can be calculated. At the macro scale, the stress intensity and the fatigue crack growth on single-crystal specimens are measured through DIC displacement and strain fields at the crack tip, also in the presence of residual strains

methods for anisotropic media [26], density functional theory (DFT) calculations, extensive digital image correlation results for displacements in crack wake and in transformation zones, we establish the modified stress intensity factor for fatigue crack growth in $Ni_{54}Fe_{19}Ga_{27}$ shape memory alloy. The elastic moduli and details of the fatigue crack growth experiments are presented in "Mate-rials, Elastic Moduli and Fatigue Crack Growth Ex-periment Details" section. In "Digital Image Correlation of the Crack Tip Strains in Cyclic Loading" section, ex-perimental determinations of strain fields at crack tips ob-tained via DIC and strain irreversibility are demonstrated.

Then, in "Method I: Extraction of Stress Intensity Factor from Displacements Using Anisotropic Elasticity via Regression" section, Method I (regression to extract effective stress intensity range) is described. In "Method II: Calculation of the Driving Force Changes Due to Transformation Shielding in Crack Wake-Equivalent Eigenstrain Determination-Minimum and Maximum Load" section, Method II (modeling to determine effective stress intensity range) is outlined and the results are extended to two other shape memory alloys. The modification in stress intensity obtained from Method I and Method II and the experimental fatigue crack growth rates are given in "Fatigue Crack

Growth Experiments and Corrections to Stress Intensity" section. Finally, in "Virtual Extensometer Results: Determination of Crack Opening Load" section, the measurements of crack opening and closure loads with virtual extensometers are presented.

Materials, Elastic Moduli, and Fatigue Crack Growth Experiment Details

Material

The material studied experimentally in this study is $Ni_{54}Fe_{19}Ga_{27}$ (hereafter referred to as Ni_2FeGa for the sake of simplicity) which undergoes cubic to tetragonal transformation (Fig. 3). It is a new class of shape memory alloys which exhibits multi-martensites with strain levels exceeding 10 % [27–29]. The materials undergoes $L2_1$ to 10 M to 14 M to $L1_0$ tetragonal transformation. The typical stress–strain response for Ni_2FeGa is summarized in Fig. 4a and b for deformation in tension. Figure 4a shows orientation dependence and the modulus difference among the three crystallographic orientations analyzed in this study. Figure 4b shows the two-stage transformation and transformation strain levels exceeding 10 %. More details are provided in Appendix 4.

Based on the lattice deformation theory calculations [30], the maximum transformation strains are known for all three orientations. Among the three orientations considered in this study, the [001] strain is as high as 12 %, while the [011] strain is 3.5 %, and the [123] strain is 4.5 %. The magnitude of the residual or accumulated strain is a fraction of the maximum strain, and based on careful measurements, we measured this strain as slightly less than 0.8 %.

The elastic moduli tensors for austenite and tetragonal martensite phases need to be known for the calculations. The austenite constants can be determined experimentally and are given in Table 4 (also graphically plotted in Fig. 5a), but the martensite elastic constants need to be evaluated from atomistic simulations. DFT calculations were made for the martensitic state ($L1_0$).

DFT Simulation Setup

In order to calculate the elastic constants of martensitic Ni_2FeGa, a cell structure consisting a total of 8 atoms was used. The cell consisted of four Ni, two Fe and two Ga atoms, thus maintaining an atomic ratio of Ni, Fe, and Ga as 2:1:1. We employed first principles calculations based on the DFT to obtain the total-energy of the system. We utilized the Vienna ab initio simulations package (VASP) with the projector augmented wave (PAW) method and the generalized gradient approximation (GGA) as implementations of DFT [31]. In our calculations, we used a 12 × 12 × 12 Monkhorst–Pack k-point meshes for the Brillouion-zone integration to ensure the convergence of results. The energy cut-off of 500 eV was used with the plane-wave basis set and a conjugate gradient algorithm was performed for ionic relaxation ensuring an energy convergence to less than 5×10^{-3} eV/Å.

To calculate the elastic constants of the martensitic ($L1_0$-non-modulated Ni_2FeGa), we obtained the total en-ergy variation of the crystal as a function of the volume subjected to six different distortions (strain). The defor-mation tensors given in Voigt notation and the corre-sponding energy densities are given in Table 2. The strain parameter δ in Table 2 for each deformation was varied from −0.03 to 0.03 in the present analysis. After obtaining the total energies E and E_0 for the strained and the un-strained lattice respectively, the parameter $(E - E_0)/V_0$ values were then plotted as a function of strain (ε), where V_0 is the equilibrium volume. The elastic constants were then extracted from the second-order coefficient fit of the following equation:

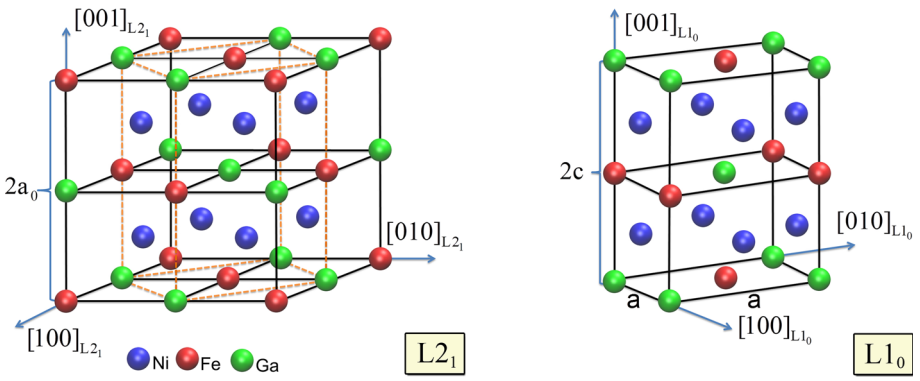

Fig. 3 The crystal lattices of cubic austenite (L21) and tetragonal martensite (L10). The lattice constants are established with DFT calculations which are then in turn used for determination of the elastic moduli tensors

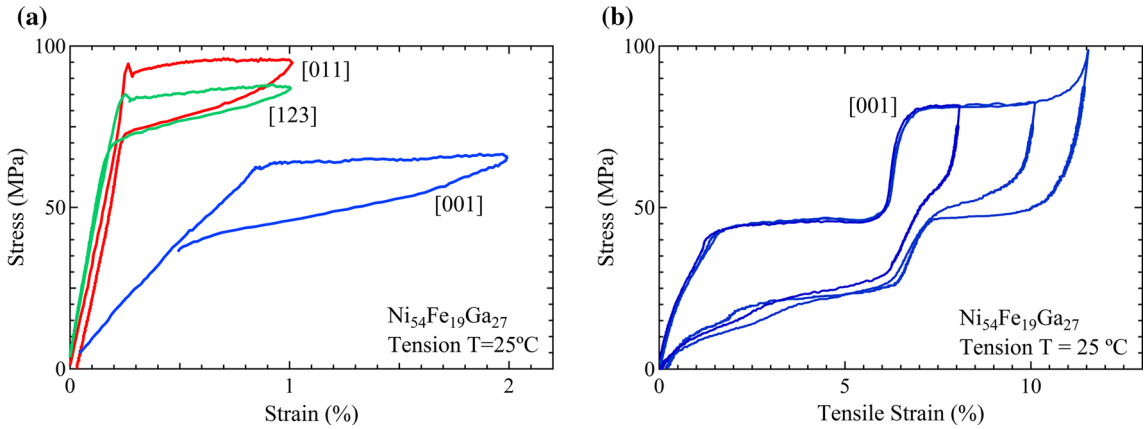

Fig. 4 **a** Stress–strain response of Ni_2FeGa in tension for three orientations considered in this study, **b** stress–strain response to high strains for the [001] case in tension. Note that the maximum transformation strains are rather high as high as 12 % in this material

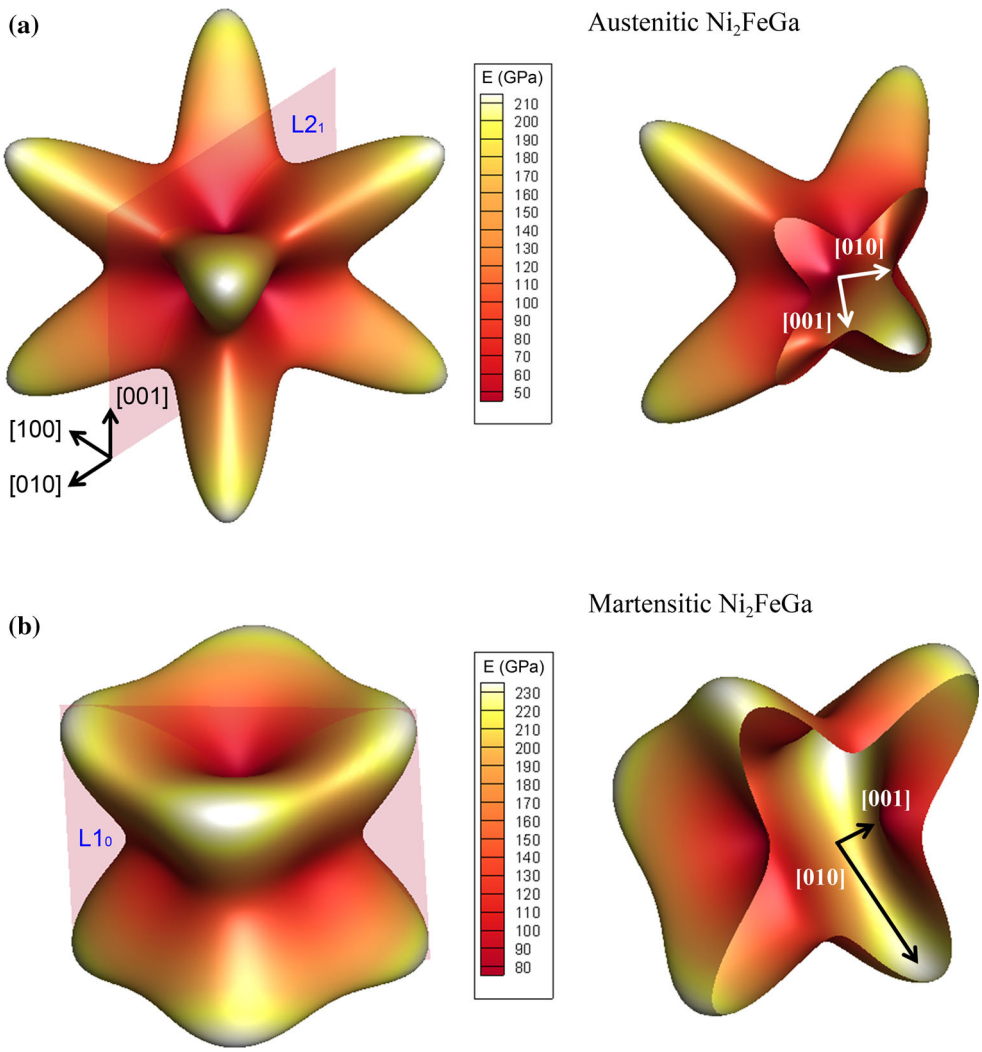

Fig. 5 Elastic moduli of Ni_2FeGa, **a** Austenite modulus as a function of crystal orientation, **b** Martensite modulus tensor, the difference in [001] and [010] represent "*c*" and "*a*" axis, respectively

Table 2 Distortion matrices and energy densities for elastic constant calculations of martensitic Ni_2FeGa

Structure	Distortion matrix	$\Delta E/V_o$
Martensite (L10)	$\varepsilon_1 = \delta^2/(1-\delta^2),\ \varepsilon_4 = \delta$	$2C_{44}\delta^2 + O(\delta^4)$
	$\varepsilon_3 = \delta^2/(1-\delta^2),\ \varepsilon_6 = \delta$	$2C_{66}\delta^2 + O(\delta^4)$
	$\varepsilon_1 = \delta,\ \varepsilon_2 = \delta,\ \varepsilon_3 = \delta^2/(1-\delta^2)$	$(C_{11} - C_{12})\delta^2 + O(\delta^4)$
	$\varepsilon_1 = \delta,\ \varepsilon_2 = \delta^2/(1-\delta^2),\ \varepsilon_3 = -\delta$	$1/2(C_{11} - 2C_{13} + C_{33})\delta^2 + O(\delta^4)$
	$\varepsilon_1 = \varepsilon_2 = \varepsilon_3 = \delta$	$(C_{11} + C_{12} + 2C_{13} + C_{33}/2)\delta^2 + O(\delta^4)$
	$\varepsilon_3 = \delta$	$(C_{33}/2)\delta^2 + O(\delta^4)$

Table 3 Elastic constants (in GPa) and the corresponding crystal structures of alloys Ni_2FeGa, NiTi, and CuZnAl in martensitic phase

Alloys	Crystal structure	C_{11}	C_{22}	C_{33}	C_{44}	C_{55}	C_{66}	C_{12}
Ni_2FeGa*	$L1_0$	256	241	212	109	109	45	103
NiTi	B19′	209	234	238	77	23	72	114
CuZnAl	18R	175	156	235	54	28	48	118
Alloys	Crystal structure	C_{13}	C_{15}	C_{23}	C_{25}	C_{35}	C_{46}	A_M
Ni_2FeGa*	$L1_0$	155	0	155	0	0	0	1.75
NiTi	B19′	102	1	139	−7	27	−5	2.5
CuZnAl	18R	40	10	150	0	0	−10	16

The data for Ni_2FeGa (marked with *) are obtained using DFT in the present analysis. The NiTi and CuZnAl data are obtained from [22, 32], respectively. The anisotropic ratios (A_M) are also given. Note the very high anisotropy ratio for CuZnAl

$$E(V,\varepsilon) = E(V_0,0) + V_0\sum_{i=1}^{6}\sigma_i\varepsilon_i + \frac{V_0}{2}\sum_{i,j=1}^{6}C_{ij}\varepsilon_i\varepsilon_j + O(\delta^3), \tag{1}$$

where C_{ij}, σ_i, ε_i are the elastic constants, stress, and strain in Voigt notation. The results are shown in Fig. 5, and the modulus tensor for martensite is provided in Table 3. The total energies to obtain $(C_{33}/2)\delta^2 + O(\delta^4)$ are discussed in Appendix 5.

In addition to the elastic moduli of martensites, the anisotropy factor is included in the Table 3. The results for NiTi and CuZnAl, two well-known studied alloys in terms of fatigue resistance, are also included in Table 3. The plots of the elastic moduli for NiTi and CuZnAl are given in Appendix 3. The NiTi results are obtained from [22] and the CuZnAl constants are obtained from [32]. The elastic constants for the three materials in the austenitic state are listed in Table 4. The anisotropy factor is also included in Table 4. The procedure for calculating the anisotropy ratio can be found in the work Ostoja-Starzewski [34]. It is important to note that these set of constants meet the mechanical stability criteria for the elastic moduli. We note that the moduli values for both austenite and martensite are strongly orientation dependent. This information is of fundamental importance for precise calculation of the internal forces acting on the crack surfaces and for determination of the stress intensity levels when displacements are measured.

Table 4 Elastic constants (in GPa) and the corresponding crystal structure of alloys in austenitic phase noted in the present study

Alloys	Crystal structure	C_{11}	C_{12}	C_{44}	A_A
Ni_2FeGa	$L2_1$	163	136	86	5.4
NiTi	B2	175	130	31	1.37
CuZnAl	B2	116	102	84	12

The data are obtained from [24, 33, 36, 37] respectively. The anisotropic ratios (A_A) for three alloys are also given

Fatigue Crack Growth Experiments

Fatigue crack growth experiments were conducted on the Ni_2FeGa single crystals for three-crystal orientations:[001], [123], and [011]. The tensile dog-bone-shaped spe-cimens utilized in this study were cut using EDM and have nominal 1.50-mm × 3-mm-gage section, 10-mm-gage length and a 0.5-mm notch. Prior to testing, the specimens were polished using SiC paper (from P800 to P1500). Successively, a fine speckle pattern adapted for image correlation was deposited using an Iwata micron B airbrush and black paint. Three experiments were conducted separately on the single crystals. The fatigue crack growth experiment on [001] $Ni_{54}Fe_{19}Ga_{27}$ was conducted under MTS Landmark Servo Hydraulic Load Frame to capture the relationship between stress intensity factor range and crack growth rate. For the other two orientations, [011] and [123], two experimental set-ups were prepared. (i) Under

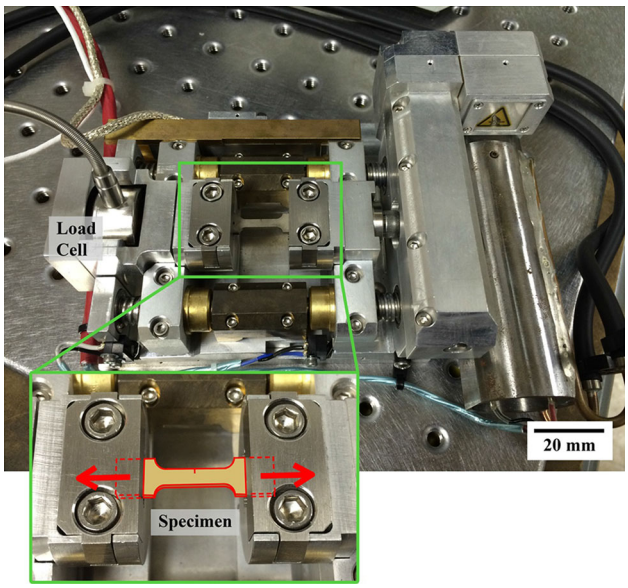

Fig. 6 The SEM tester that is utilized with high resolution microscope to measure the local crack tip displacements for fatigue experiments

the same servo hydraulic load frame, we initially pre-cracked the specimens utilizing constant amplitude loadings in order to induce a fatigue crack from the notch. For this experimental configuration, the images used for crack length measurements and displacements (in x and y directions) and strain fields correlations were captured using an IMI model IMB-202 FT CCD camera (1600 × 1200 pixel) with a Navitar optical lens, providing an average resolution of approximately 2 μm/px [35]. (ii) Successively, the cracked specimens were loaded under a 4.5 kN EBSD SEMTester which was herein fitted under an Olympus BX51M microscope (Olympus lens). This set-up is shown in Fig. 6 and was utilized for obtaining images at higher magnifications (from 0.44 up to 0.22 μm/px). This set-up allows precisely obtaining the strains at crack tip and the extent of the residual transformation zone. For these three experiments, initial images of the virgin specimens were captured prior to loading (reference images) in order to calculate the accumulated strain in the further analyses.

Digital Image Correlation of the Crack Tip Strains in Cyclic Loading

Displacement and strain fields were monitored in the vicinity of the crack as the crack advances. These measurements were made at maximum load, minimum load, and at intermediate loads. As the crack advances into a zone of transformed material is generated in the wake of the crack. This zone height and the strains are readily measured from the digital image correlation results. An example of the strains in the crack wake is shown in Figs. 7 and 8. In Fig. 7, the axial strain fields at the beginning of the cycle (point A) and at the end of the cycle (point B) are shown for the [011] crystal orientation. The strain maps were obtained adopting two image resolutions. Utilizing the 0.44 μm/px set-up the full-field strain field of the notch region can be analyzed, and the extent of the crack wake can be readily obtained. Images captured at higher resolutions (0.22 μm/px for the example reported) are then necessary in order to characterize the crack-tip strain field. From the high-resolution strain fields marked as A and B in Fig. 7, it is possible to calculate the accumulation of the local strains in front of the crack tip following the fatigue cycle.

Providing these strain measurements for different crack lengths, in Fig. 8, we report the strain accumulation during crack propagation in terms of the equivalent strain at the crack tip. The equivalent strain at the crack tip was calculated via averaging the strain tensor components over a region of approximately 50 μm × 50 μm in front of the crack tip for different crack lengths. That is, within this confined region ahead of the crack tip, the strain components, e_{xx}, e_{yy}, and e_{xy}, can be extracted from digital image correlation results. Consequently, the corresponding equivalent strain, $e_{\text{Equivalent}}$, can be calculated from Eq. (2). The difference between levels of strain at point A and point B, in Fig. 8, yields the equivalent strain accumulation in one fatigue cycle

$$e_{\text{Equivalent}} = \sqrt{\frac{2}{3}\left(e_{xx}^2 + 2e_{xy}^2 + e_{yy}^2\right)}. \tag{2}$$

A comparison of the strain fields at peak and minimum load for the three crystal orientations [001], [123], and [011] is illustrated in Fig. 9. The shapes of the transfor-mation region determined using these strain fields will be used to evaluate the reduction in stress intensity factor for each orientation.

Stress Intensity Determination via Regression and Modeling, Fatigue Crack Growth Rates, Virtual Extensometers, and Key Variables for Modeling

Method I: Extraction of Stress Intensity Factor from Displacements Using Anisotropic Elasticity via Regression

The displacement fields from the digital image correlation are shown in Fig. 10. In Figs. 10a and b, the displacements normal and parallel to the crack tip are shown respectively for fatigue crack growth in [001] oriented specimens. These results are fitted to the anisotropic displacement fields for cubic crystals. Such solutions are available by Sih

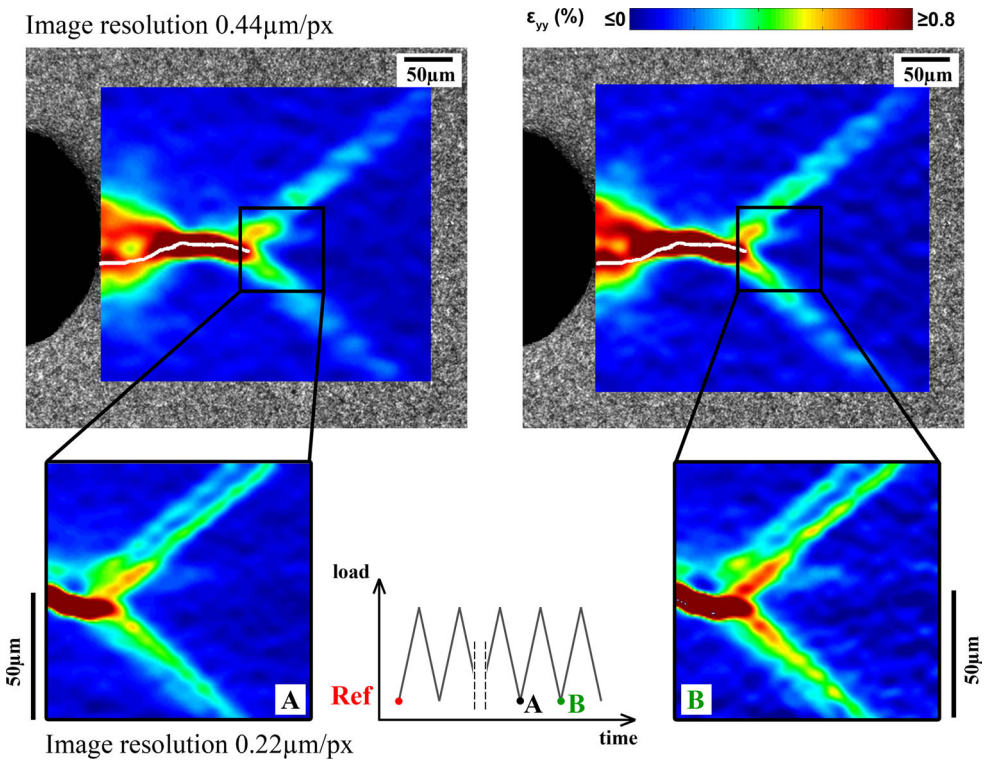

Fig. 7 Residual strain accumulation during cycling loading of Ni_2FeGa oriented along the [011] crystal direction; the DIC images are taken at minimum load at the beginning of the cycle (point A) and at the conclusion of the cycle (point B) and correlated with the reference image

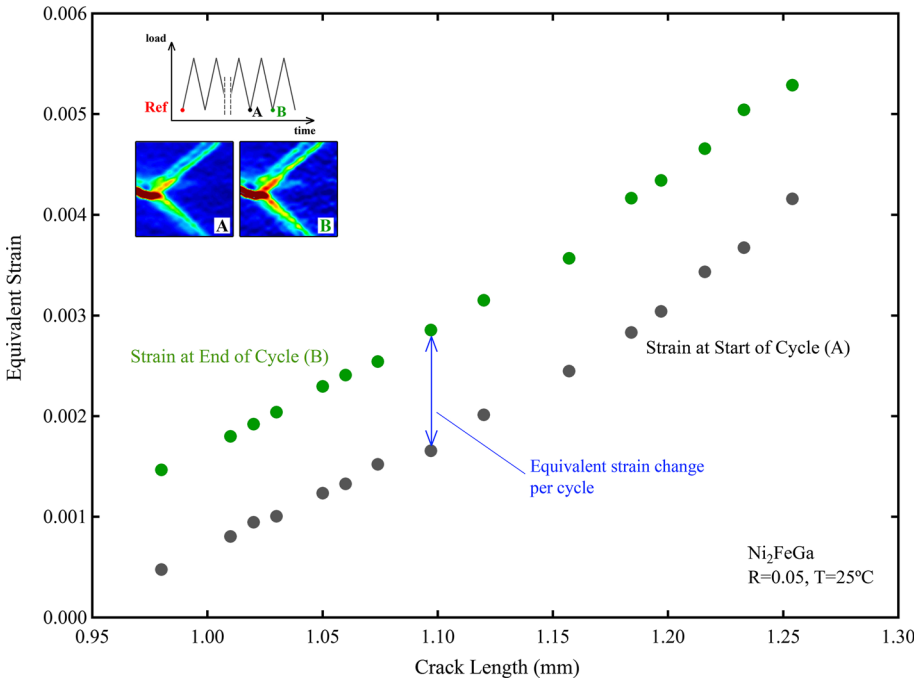

Fig. 8 The measured accumulation of equivalent strains over a wide range of crack lengths. The accumulated strain per cycle is the difference between the strain levels at points B and A shown in the schematic

et al. [26]. It is possible to extract the stress intensity by regression fit to the following set of equations, Eqs. (3) and (4). We note that the equations include the elastic constants and T stress term. We also note that the orientation of the crack in the [001] specimen is 45° to the loading axis. In this case, both Mode I and Mode II stress intensities can be extracted. In the case of [123] and [011]-oriented single crystals, the crack grew nearly normal to the loading axis and the Mode II stress intensity is small. The crack tip displacements for the [123]-oriented specimens are shown in Fig. 10c. Figures 10a–c demonstrate the comparison between experimental and regression displacement fields.

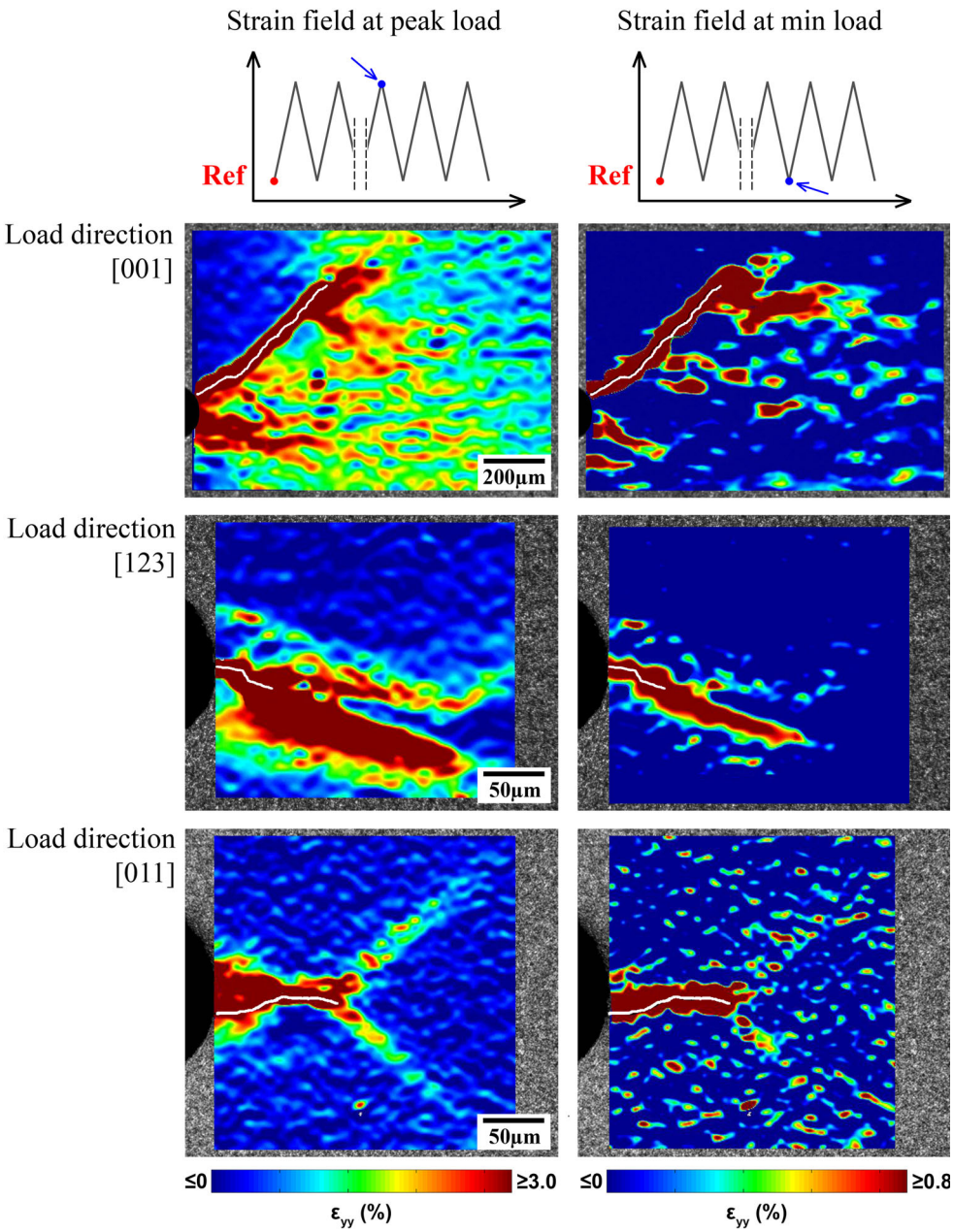

Fig. 9 The strain fields at the peak and at the minimum loads obtained from fatigue crack growth experiments on Ni_2FeGa utilizing digital image correlation. The results for fatigue loading in three orientations are displayed: [001], [123], and [011]

A video was attached to this paper to illustrate such comparison during one fatigue cycle.

The stress intensity factors, K_1 and K_2, can be extracted from horizontal and vertical displacements, u^1 and v^1, through the following equations

$$u^1 = K_1\sqrt{2r}\mathrm{Re}\left[\frac{1}{\mu_1-\mu_2}\left(\mu_1 p_2\sqrt{\cos\theta+\mu_2\sin\theta}\right.\right.$$
$$\left.\left.-\mu_2 p_1\sqrt{\cos\theta+\mu_2\sin\theta}\right)\right] + K_2\sqrt{2r}\mathrm{Re}$$
$$\left[\frac{1}{\mu_1-\mu_2}\left(p_2\sqrt{\cos\theta+\mu_2\sin\theta}-p_1\sqrt{\cos\theta+\mu_2\sin\theta}\right)\right]$$
$$+a_{11}\mathrm{Tr}\cos\theta+\mathrm{Ar}\sin\theta+B_u \qquad (3)$$

$$v^1 = K_1\sqrt{2r}\mathrm{Re}\left[\frac{1}{\mu_1-\mu_2}\left(\mu_1 q_2\sqrt{\cos\theta+\mu_2\sin\theta}\right.\right.$$
$$\left.\left.-\mu_2 q_1\sqrt{\cos\theta+\mu_2\sin\theta}\right)\right]$$
$$+K_2\sqrt{2r}\mathrm{Re}\left[\frac{1}{\mu_1-\mu_2}\left(q_2\sqrt{\cos\theta+\mu_2\sin\theta}\right.\right.$$
$$\left.\left.-q_1\sqrt{\cos\theta+\mu_2\sin\theta}\right)\right]$$
$$+a_{12}\mathrm{Tr}\cos\theta+\mathrm{Ar}\sin\theta+B_v \qquad (4)$$

$$a_{11}\mu^4-2a_{16}\mu^3+(2a_{12}+a_{66})\mu^2-2a_{26}\mu+a_{22}=0, \qquad (5)$$

where Re represents the real part of a complex number, T is the T-stress, A is the rigid body rotation, B_u and B_v are the

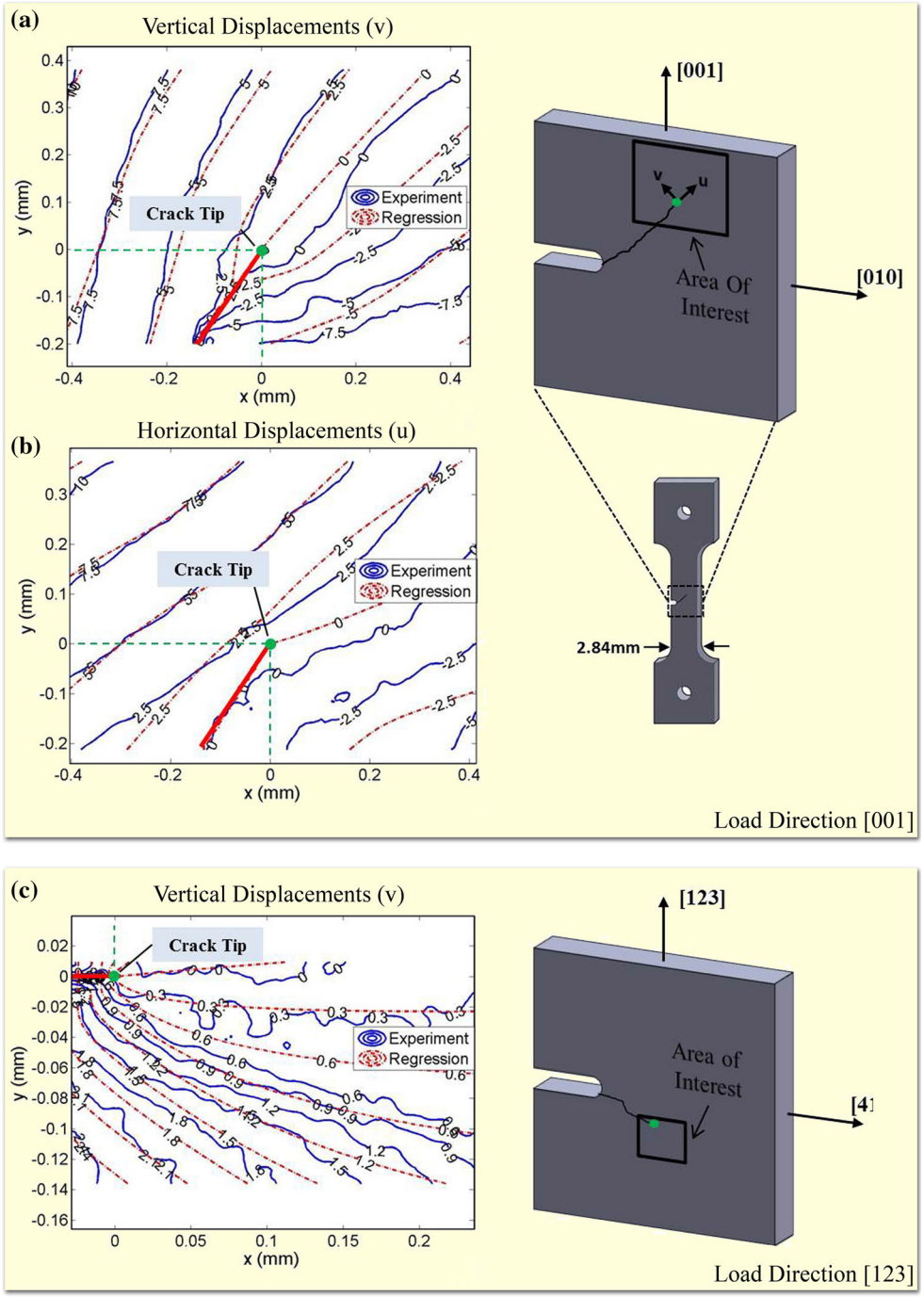

Fig. 10 The crack tip displacements. **a** Normal to the crack plane (indicated as vertical displacements v), and **b** horizontal to the crack plane (horizontal displacements u) for the inclined crack in a single-crystal oriented in [001] orientation. **c** The vertical crack tip displacements for the single crystal oriented in [123] orientation

rigid body translations in u^1 and v^1 directions, respectively, a_{11}, a_{12}, a_{16}, a_{22}, a_{26}, and a_{66} are the compliance components, r and θ are the polar coordinates with their origin at the crack tip, and μ_1 and μ_2 are the roots of Eq. (5). The p_i and q_j in Eqs. (3) and (4) are the anisotropic terms defined in the following ways

$$p_i = a_{11}\mu_i^2 + a_{12} - a_{16}\mu_i$$
$$q_j = a_{12}\mu_j + \frac{a_{22}}{\mu_j} - a_{26}. \tag{6}$$

Method II: Calculation of the Driving Force Changes Due to Transformation Shielding in Crack Wake-Equivalent Eigenstrain Determination-Minimum and Maximum Load

The strain level measured via DIC is shown in Fig. 9 for different single-crystal orientations. Since the transformed area is surrounded by the matrix material, the DIC result can be interpreted as the total strain, e^t_{mn} which is the sum of constrained strain and far field strain. The intrinsic

transformation strain, e^p_{kl} can be calculated by following equation

$$e^p_{kl} = S^{-1}_{klmn}\left(e^t_{mn} - e^o_{mn}\right), \tag{7}$$

where e^o_{mn} is the far-field strain and S_{ijkl} the Eshelby's tensor for cubic crystal material. The S_{ijkl} represents the geometry of the martensite platelets and is treated as a flat ellipsoidal shape. It can be obtained as

$$S_{ijkl} = \frac{1}{8\pi} C_{pqkl}\left(\bar{G}_{ipjq} + \bar{G}_{jpiq}\right), \tag{8}$$

where the specific terms, $\bar{G}_{ipjq}$, are given a book by Mura [38] and also in Appendix 1 for completeness.

Assuming the minimum load to be near zero, the misfit strain due to modulus mismatch can be neglected. As a result, in the case of minimum load, e^p_{kl} is the equivalent eigenstrain that needs to be calculated. Therefore, the corresponding stress, T_{ij}, on the transformation contour can be obtained via

$$T_{ij} = C_{ijkl} e^p_{kl}. \tag{9}$$

When the maximum load is applied, the eigenstrain effect due to modulus mismatch, e^*_{mn} needs to be taken into account. The equivalent eigenstrain, e^{**}_{mn}, which is the sum of e^*_{mn} and e^p_{kl} can be calculated through Eshelby's equivalent method described below

$$\begin{aligned} &C_{ijkl}\left(e^0_{kl} + S_{klmn}e^{**}_{mn} - e^{**}_{kl}\right) = C'_{ijkl}\left(e^0_{kl} + S_{klmn}e^{**}_{mn} - e^p_{kl}\right) \\ &e^{**}_{mn} = \left[\left(C_{ijkl} - C'_{ijkl}\right)S_{klmn} - C_{ijmn}\right]^{-1} \\ &\times \left[\left(C_{ijkl} - C'_{ijkl}\right)e^0_{kl} - C_{ijkl}e^p_{kl}\right], \end{aligned} \tag{10}$$

where C_{ijkl} and C'_{ijkl} are the elastic moduli of cubic austenite and tetragonal martensite for Ni_2FeGa, respectively. These tensors are given in "DFT Simulation Setup" section. We note that all tensors are given in the cubic coordinate frame, and the rotations associated with the transformation are accounted for when the moduli are determined.

Upon calculation of the equivalent eigenstrains, the corresponding stress, T_{ij}, in the transformation zone can be ascertained as

$$T_{ij} = C_{ijkl} e^{**}_{kl} \tag{11}$$

Using equation above, it is possible to determine the internal tractions along the transformation contour using the Cauchy formula. Further details are given in Appendix 1.

Knowing the tractions on the surface of transformation zone, we can numerically calculate the stress intensity change for a specific loading case. By implementing the weight function technique proposed by Bueckner and Rice [4], the stress intensity factor due to the internal tractions, ΔK_I, can be written as

$$\Delta K_I = \int_{S_p} n_i T_{ij} h_j \mathrm{d}S_\mathrm{p}, \tag{12}$$

where n_i is the outward normal of the transformation zone, $\mathrm{d}S_\mathrm{p}$ is the line element on the perimeter of the zone, and h_j is the anisotropic weight function which is going to be determined.

According to Rice, the weight function can be readily obtained through Eq. (13) if the displacement fields, u^1 and v^1, and stress intensity factor, K_1 and K_2, in a reference load system are known

$$\begin{aligned} h_x &= \frac{H}{2K_1}\frac{\partial u^1}{\partial l} \\ h_y &= \frac{H}{2K_1}\frac{\partial v^1}{\partial l}. \end{aligned} \tag{13}$$

The solution for stress intensity factors due to tractions on the crack surface in Fig. 11 can be found via Eq. (14) and displacement fields are provided by Sih et al. [26] as

$$\begin{aligned} K_1 &= -\frac{1}{\pi\sqrt{a}}\int_0^a \sigma(x)\left[\sqrt{\left(\frac{a+x}{a-x}\right)} - \frac{1}{2}\frac{\alpha_o}{\beta_o}\right]\mathrm{d}x \\ K_2 &= -\frac{1}{\pi\sqrt{a}}\int_0^a \sigma(x)\left\{\frac{\alpha_o^2}{2\beta_o} + \frac{1}{2\beta_o}\left[\frac{a_{12}}{a_{11}} + \left(\alpha_o^2 + \beta_o^2\right)\right]\right\}\mathrm{d}x, \end{aligned} \tag{14}$$

where α_o and β_o are the real and imaginary component of the roots for Eq. (5), i.e., for $\mu_1 = \alpha_o + \beta_o i$ and $\mu_2 = -\alpha_o + \beta_o i$.

The elastic moduli, H, can be represented in Eq. (15)

$$H = -\frac{1}{8}\left(\frac{\mu_1 - \mu_2}{\mu_2}\right)\left\{\frac{i}{\alpha_o\beta_o}\left[\frac{a_{12}}{a_{11}} + \left(\alpha_o^2 - \beta_o^2\right)\right] + 1\right\}. \tag{15}$$

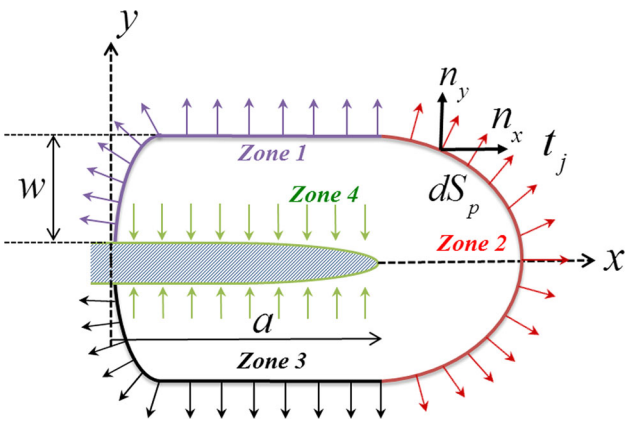

Fig. 11 Schematic of the load system on the crack surface. Four zones are considered and the contributions of all four zones are taken into account. Zones 1, 3 and 4 have the most significant influence on the results of stress intensity due to internal tractions

Once weight functions are obtained, the corresponding stress intensity factor in that loading system can be determined through Eq. (13). The summation of stress intensity factors obtained from different parts of the transformation contour (Fig. 11) yields the change of stress intensity factor due to transformation effect. Further details are given in Appendix 2.

The net reduction in stress intensity factor as the applied loading is increased is given in Table 5. The contributions from different sectors of the transformation zone are provided. It is noted that the Zone 2 provides negligible contribution while Zones 1 and 3 provide a smaller contribution compared to Zone 4. These results are further presented in the next section.

Fatigue Crack Growth Experiments and Corrections to Stress Intensity

The experimental fatigue crack growth rate results and predictions of fatigue crack growth rates upon correction of stress in intensity range are shown in Fig. 12. The effective stress intensity range upon regression of the entire displacement field is also included in Fig. 12. The agreement for the theory and regression-based stress intensity range is excellent. The reduction in the stress intensity range is approximately 35 % of the full range based on regression and also based on theory. We show virtual extensometer results of crack opening displacements confirming the crack closure in the next section.

Virtual Extensometer Results: Determination of Crack Opening Load

The virtual extensometer method is another technique for determining the crack closure levels which is complimentary to 'regression.' The technique is illustrated in Fig. 13a. The relative displacements across the crack faces are measured during loading and unloading. Therefore, DIC measurements allow the determination of the crack opening displacements during loading and unloading. By making such measurements over fine increments, it is possible to precisely determine the applied load level at which the crack opening occurs. These results are shown in Fig. 13b for two crack lengths. The crack opening load is determined as 35 % of the maximum load.

Sensitivity of Results to a/w Ratio and the Moduli Levels

Three other shape memory alloys were assessed to evaluate the propensity of K reduction. The results are shown in Tables 6 and 7. In the first set of simulations (Table 6), the a/w ratio was maintained at 2. In Table 7, we consider the reductions in K at both maximum and minimum loads for different a/w ratios. A noteworthy point is that the reduction in K occurs at both maximum and minimum load. However, since the reduction is higher at the maximum load, this results in a net decrease in stress intensity range.

The sensitivity of the simulations on the variations in the a/w ratio and martensite moduli magnitude is studied in Fig. 14a and b. The basis for these simulations is the Ni_2-FeGa alloy. We note that as the a/w ratio increases, with all other parameters constant, the reduction in both minimum and maximum stress intensity is noted. The overall reduction in stress intensity range saturates with increasing a/w ratio. In Fig. 14b, the martensite modulus is premultiplied by a factor. The factor $F = 1$ corresponds to the Ni_2FeGa case. As the factor increases the reduction in stress intensity range increases.

Discussion of Results

Fatigue crack growth experiments were conducted on the new Ni_2FeGa shape memory alloy. Extensive experimental results and measurements for fatigue crack growth were obtained in the course of this study. Three single-crystal orientations of Ni_2FeGa shape memory alloy were tested in tension–tension fatigue. The experimental results were obtained at room temperature where the material deforms under 'pseudoelastic' conditions. The crack advance was measured as a function of the effective stress intensity range and the threshold stress intensity range was precisely established as 8.3 $\mathrm{MPa}\sqrt{\mathrm{m}}$.

Table 5 Stress intensity factor (K ($\mathrm{MPa}\sqrt{\mathrm{m}}$)) values due to tractions on different zone boundaries of Ni_2FeGa in Fig. 11 for the $a/w = 2$ case

Zone # Load (MPa)	Zone 1 K_1	Zone 2 K_2	Zone3 K_3	Zone 4 K_4	Total $K_{\mathrm{red}} = \sum K_i (\mathrm{MPa}\sqrt{\mathrm{m}})$
3.34	0.35	0.013	0.35	−3.07	−2.37
10	0.42	0.018	0.42	−3.69	−2.85
20	0.63	0.023	0.63	−4.75	−3.49
30	0.93	0.028	0.93	−7.03	−5.17
40	1.16	0.033	1.16	−8.75	−6.43
50	1.46	0.039	1.46	−10.9	−7.98

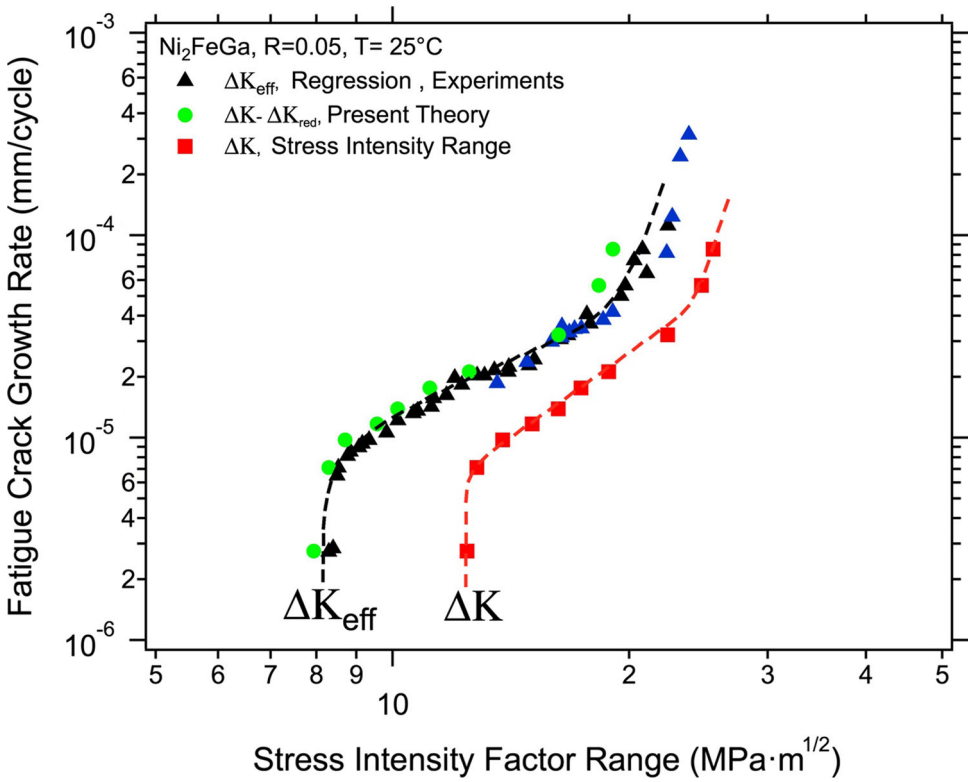

Fig. 12 Fatigue crack growth behavior of primarily based on experiments on [001] single crystals. The range in effective stress intensity is obtained by regression analysis of crack tip displacements (present experiments) and also via calculation of the shielding effects due to transformation (present theory). The effective threshold stress intensity range is 8.3 MPa$\sqrt{\text{m}}$. The full range of stress intensity is also provided as a reference. The *dashed lines* are drawn to aid the eye

Reduction in stress intensity range (of the order of 30 %) was established by calculating the closure forces (Method II —"Method II: Calculation of the Driving Force Changes Due to Transformation Shielding in Crack Wake-Equivalent Eigenstrain Determination-Minimum and Maximum Load" section) via a micro-mechanical analysis. The closure forces arise due to residual strains in the wake of the crack. The calculated crack tip stress intensity range is in agreement with the experimental measurements of the effective stress intensity range. We used two experimental measurements for measuring the effective stress intensity range. In the first one, the crack tip displacement fields were utilized to establish the stress intensity range with a least square fitting procedure (Method I—"Method I: Ex-traction of Stress Intensity Factor from Displacements Using Anisotropic Elasticity via Regression" section). This method resulted in establishment of the effective stress intensity range 30 % smaller than the theoretical one. The difference is attributed to shielding due to residual dis-placements in the crack wake. In the second one, by using virtual extensometers along the crack faces ("Virtual Ex-tensometer Results: Determination of Crack Opening Load" section), the crack opening and crack closure loads were measured and found to be also at nearly 30 % of the maximum load.

A combined experimental-theoretical methodology is outlined for a better understanding of the driving force for fatigue crack growth in shape memory alloys. The choice of single crystals allowed precise knowledge of the elastic moduli in the austenitic and martensitic phases. In turn, the moduli tensors were used in a micro-mechanical analysis to determine the equivalent eigenstrains in the transformed regions. The equivalent eigenstrain was used to determine the internal tractions at maximum load of the cycle. This led to the calculation of the reduction in stress intensity, hence a modified range of stress intensity was determined. The calculations presented represent an advancement by accounting for elastic moduli difference and with the experimental determination of strain fields at minimum and maximum loads.

To put perspective on the results, the simulations were repeated on two well-known shape memory materials, the NiTi and CuZnAl. The reductions in stress intensity range were lower in NiTi compared to Ni_2FeGa, while the reduction in CuZnAl was substantially lower than NiTi and Ni_2FeGa. These results cannot be directly compared with experiments in the literature, since there is no reported CuZnAl fatigue crack growth data to our knowledge. The literature on NiTi shows threshold levels that are lower compared to Ni_2FeGa.

Fatigue crack growth behavior in shape memory alloys remains a complex topic. The elastic moduli evolves continuously; it is strongly orientation dependent in both austenite and martensite. The moduli tensors decide the equivalent eigenstrains, hence the closure forces. The closure forces vary as a function of cycles accompanying the

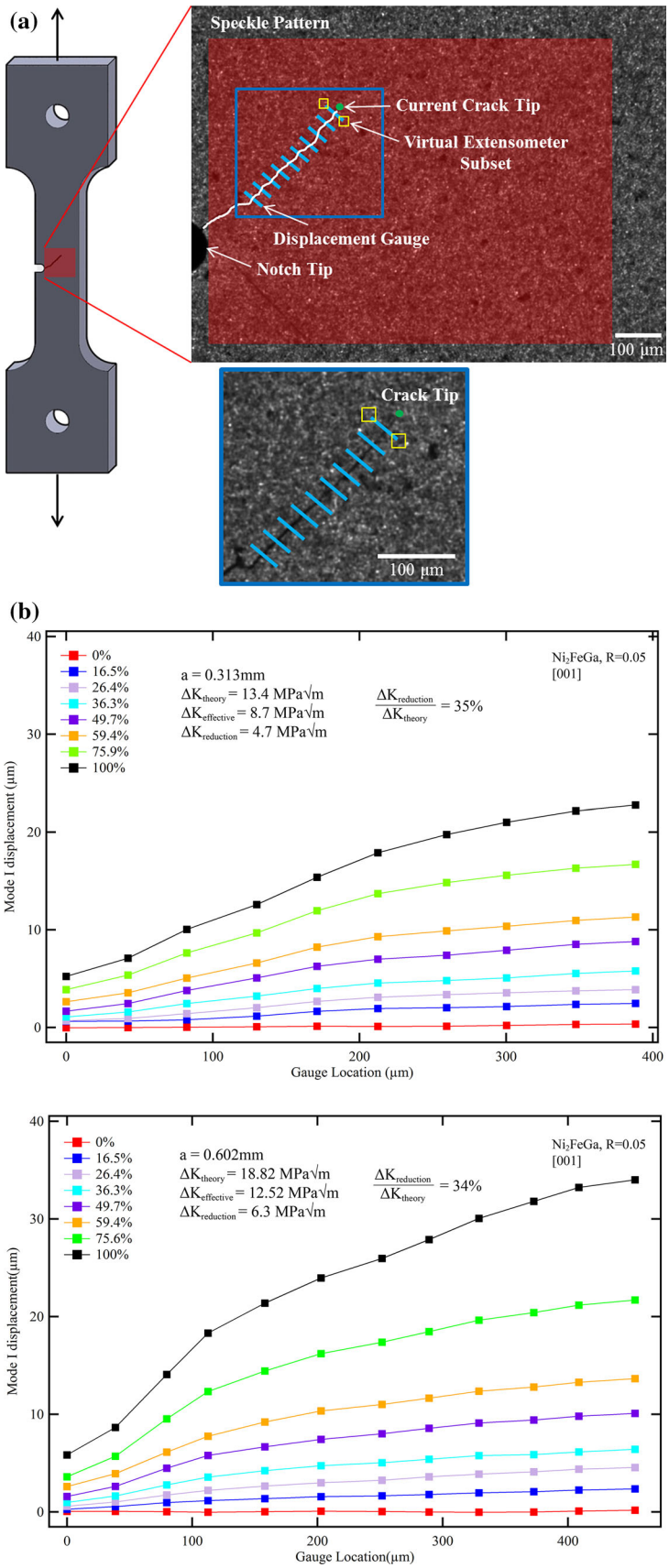

Fig. 13 **a** Schematic of the virtual extensometer methodology used for crack closure measurements. **b** The crack opening displacement profiles, utilizing virtual extensometers, for the specimen oriented in [001] direction. The gage location is the distance behind the crack tip. The profiles are given as a fraction of the maximum applied load. The crack opening load is determined as 35 % of the maximum applied load

Table 6 The $\Delta K_{red}(\mathrm{MPa}\sqrt{\mathrm{m}})$ values for alloys noted in the present study

Alloys	a/w	$\Delta K_{red}(\mathrm{MPa}\sqrt{\mathrm{m}})$
Ni_2FeGa	2	−5.61
NiTi	2	−2.38
CuZnAl	2	−1.91

Table 7 Reduction in stress intensity factor ($K_{red}(\mathrm{MPa}\sqrt{\mathrm{m}})$) values for alloys noted in the present study at minimum and maximum loads

Alloys	a/w	$K_{red-min}$ Minimum load	$K_{red-max}(\mathrm{MPa}\sqrt{\mathrm{m}})$ Maximum load
NiTi	0.5	−1.05	−2.59
	1	−1.47	−3.37
	2	−1.8	−4.18
	4	−2.25	−4.54
Ni_2FeGa	0.5	−1.26	−3.06
	1	−1.89	−6.74
	2	−2.59	−7.34
	4	−3.17	−7.77
CuZnAl	0.5	−1.48	−2.81
	1	−1.86	−3.5
	2	−2.29	−4.2
	4	−2.62	−4.7

residual transformation strains. In this study, we established the modification in stress intensity and established a rigorous estimate of the stress intensity range. In future studies, the crack growth rate needs to be predicted based on the magnitude of the irreversibility in displacements at crack tips [39, 40]. This would require knowledge of the slip and transformation energy barriers in the material [41]. This approach would need to be taken with care because both transformation and plasticity can occur simultane-ously at the crack tips. In the present calculations no ex-plicit consideration of plastic slip was included [41]. Plasticity can occur at high stress levels and it needs to be considered in future work.

Finally, we comment on the role of martensite to austenite modulus change. Evidence of higher martensite modulus relative to austenite is well documented [42]. On the other hand, the martensite modulus is taken as less than the austenite modulus in most constitutive models. The martensite moduli upon deformation in fatigue and fracture studies are the oriented martensite and not the self-accomodated one [22]. Also, the constitutive models utilized have been simple for the ease of implementation in FEM codes. This creates some difficulty when residual strain buildup due to residual martensite or plastic deformation needs to be considered. There is no provision for these

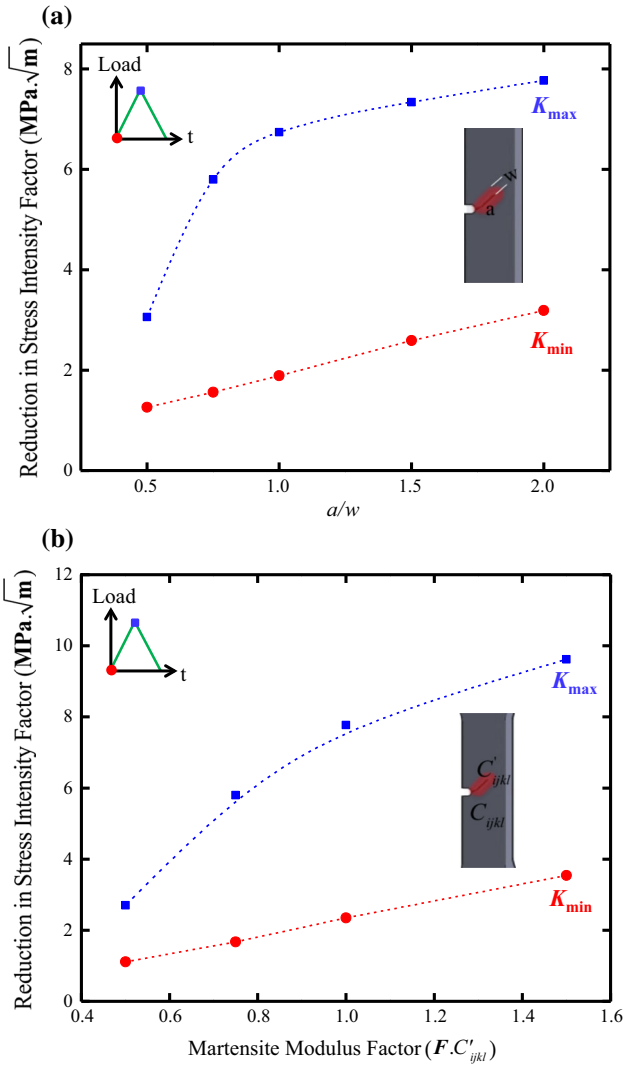

Fig. 14 **a** Reduction in maximum and minimum stress intensity levels with increase in crack length, the results are for the [001] Ni_2FeGa material and explore the hypothetical variation of residual transformation zone on the results. **b** Reduction in maximum and minimum stress intensity levels as a function of martensite modulus factor. The moduli tensor is simply scaled by the factor, F. The $F = 1$ case corresponds to the baseline Ni_2FeGa material

mechanisms in most constitutive models. Finally, there is the matter of orientation dependence. A highly anisotropic material cannot be represented accurately as isotropic with two elastic constants. Constitutive models will need to incorporate these characteristics.

Conclusions

The work supports the following conclusions:

(1) The new shape memory alloy Ni_2FeGa displays unusually high fatigue thresholds (8.3 $\mathrm{MPa}\sqrt{\mathrm{m}}$) and excellent fatigue crack growth resistance. The

reduction of the stress intensity range associated with the transformation is considerable as shown with an anisotropic micro-mechanics calculation.

(2) Excellent quantitative correlation is achieved between theory and the experimental measurements of stress intensity range reduction. Utilizing crack tip displacement fields with digital image correlation methods allowed evaluation of the effective stress intensity range in agreement with the virtual extensometers along the crack flanks. These results show that the reduction in stress intensity is 35 % of the full range.

(3) Comparisons were made between three shape memory alloys to assess their propensity for shielding associated with phase transformations. It was found that the Ni_2FeGa produced higher levels of stress intensity reduction compared to NiTi and CuZnAl alloys. The work underscored the role of elastic moduli in the martensitic and austenitic phases on the calculations of the reduction in stress intensity range.

Acknowledgments The work was supported by Nyquist Chair funds at University of Illinois. The authors acknowledge the assistance of Mr. George Li.

Appendix 1: Eshelby Tensor for Anisotropic Media

The treatment follows that given by Mura [38]. The Eshelby's tensor calculation is introduced in Eq. (8)

$$S_{ijkl} = \frac{1}{8\pi} C_{pqkl}\left(\bar{G}_{ipjq} + \bar{G}_{jpiq}\right).$$

For the case of cubic material, the definition of $\bar{G}_{ipjq}$ is presented in Eq. (16)

$$\begin{aligned}
\bar{G}_{1111} &= \bar{G}_{2222} = \frac{2\pi}{a}\int_0^1 \frac{(1-x^2)}{pq}\left(1-x^2+\rho^2x^2\right) \\
&\times \left[\mu^2(1-x^2+\rho^2x^2)+\beta\rho^2x^2\right]\mathrm{d}x \\
&+\frac{\pi}{a}\int_0^1 \frac{(1-x^2)^2}{p(p+q)}\left[\beta\left(1-x^2+\rho^2x^2\right)+\gamma\rho^2x^2\right]\mathrm{d}x \\
\bar{G}_{3333} &= \frac{4\pi}{a}\int_0^1 \frac{\rho^2x^2}{pq}\left(1-x^2+\rho^2x^2\right)\left[\mu^2(1-x^2+\rho^2x^2)\right. \\
&\left.+\beta\left(1-x^2\right)\right]dx+\frac{\pi\gamma}{a}\int_0^1 \frac{\rho^2x^2(1-x^2)^2}{p(p+q)}\mathrm{d}x \\
\bar{G}_{1122} &= \bar{G}_{2211} = \frac{2\pi}{a}\int_0^1 \frac{(1-x^2)}{pq}\left\{\left(1-x^2+\rho^2x^2\right)\right. \\
&\left[\mu^2(1-x^2+\rho^2x^2)+\beta\rho^2x^2\right]+\left(1-x^2\right) \\
&\left.\left[\beta\left(1-x^2+\rho^2x^2\right)+\gamma\rho^2x^2\right]\right\}\mathrm{d}x \\
&-\frac{\pi}{a}\int_0^1 \frac{(1-x^2)^2}{p(p+q)}\left[\beta\left(1-x^2+\rho^2x^2\right)+\gamma\rho^2x^2\right]\mathrm{d}x\bar{G}_{1133} = \bar{G}_{2233} \\
&= \frac{2\pi}{a}\int_0^1 \frac{\rho^2x^2}{pq}\left\{2\left(1-x^2+\rho^2x^2\right)\right. \\
&\left[\mu^2(1-x^2+\rho^2x^2)+\beta\rho^2x^2\right]+\left(1-x^2\right) \\
&\left.\left[\beta\left(1-x^2+\rho^2x^2\right)+\gamma\rho^2x^2\right]\right\}\mathrm{d}x\bar{G}_{1212} \\
&= -\frac{\pi(\lambda+\mu)}{a}\int_0^1 \frac{(1-x^2)^2}{p(p+q)}\left[\mu\left(1-x^2+\rho^2x^2\right)+\mu'\rho^2x^2\right]\mathrm{d}x
\end{aligned} \tag{16}$$

$$\begin{aligned}
\bar{G}_{1313} &= \bar{G}_{2323} \\
&= -\frac{2\pi\mu(\lambda+\mu)}{a}\int_0^1 \frac{\rho^2x^2(1-x^2)(1-x^2+\rho^2x^2)}{pq}\mathrm{d}x \\
&\quad -\frac{\pi\mu'(\lambda+\mu)}{a}\int_0^1 \frac{\rho^2x^2(1-x^2)^2}{p(p+q)}\mathrm{d}x \\
\bar{G}_{3311} &= \bar{G}_{3322} \\
&= \frac{2\pi}{a}\int_0^1 \frac{(1-x^2)}{pq}\left(1-x^2+\rho^2x^2\right)\left[\mu^2(1-x^2+\rho^2x^2)\right. \\
&\quad \left.+\beta\left(1-x^2\right)\right]\mathrm{d}x \quad +\frac{\pi\gamma}{2a}\int_0^1 \frac{(1-x^2)^3}{p(p+q)}\mathrm{d}x.
\end{aligned}$$

Specific terms in Eq. (16) can be represented as the following,

$$\begin{aligned}
&\rho = a_1/a_3 \\
&a = \mu^2(\lambda+2\mu+\mu') \\
&b = a^{-1}\mu\mu'(2\lambda+2\mu+\mu') \\
&c = a^{-1}\mu'^2(3\lambda+3\mu+\mu') \\
&\beta = \mu(\lambda+\mu+\mu') \\
&\gamma = \mu'(2\lambda+2\mu+\mu') \\
&p = \left\{\left(1-x^2+\rho^2x^2\right)^3+b\rho^2x^2\left(1-x^2\right)\left(1-x^2+\rho^2x^2\right)\right. \\
&\quad \left.+\frac{1}{4}\left(1-x^2\right)^2\left[b\left(1-x^2+\rho^2x^2\right)+c\rho^2x^2\right]\right\}^{\frac{1}{2}}, \quad 0<x<1 \\
&q = \left\{\left(1-x^2+\rho^2x^2\right)^3+b\rho^2x^2\left(1-x^2\right)\left(1-x^2+\rho^2x^2\right)\right\}^{\frac{1}{2}}, \\
&\quad 0<x<1,
\end{aligned} \tag{17}$$

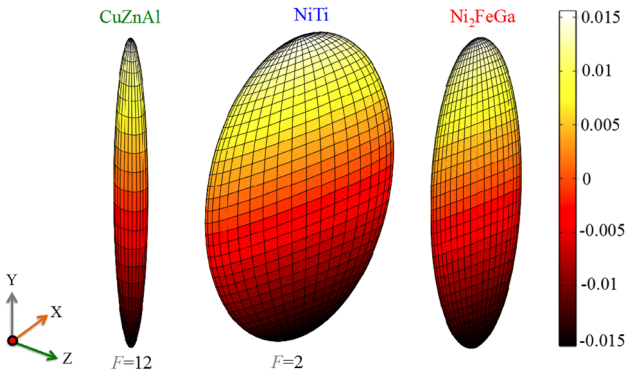

Fig. 15 The principal equivalent eigenstrains for three materials (CuZnAl, NiTi and Ni_2FeGa). The factor F is applied to NiTi and CuZnAl indicating that the magnitude of the strains are smaller in those two materials

where λ is C_{12}, μ is C_{44}, μ' is C_{11}–C_{12}–2C_{44}, a_1, a_2, and a_3 are the semi axis align with the coordinate x, y and z. For the case of flat ellipsoid ($a_1 > a_2 > a_3$), ρ is assumed to be infinity (Fig. 15).

Appendix 2: The Weight Functions

Earlier, the calculation of weight function was introduced as the following.

$$h_x = \frac{H}{2K_1}\frac{\partial u^1}{\partial l}$$
$$h_y = \frac{H}{2K_1}\frac{\partial v^1}{\partial l} \tag{18}$$

Horizontal displacement u^1 and vertical displacement v^1 can be found earlier. The stress intensity factor K_1 is presented earlier as well as the elastic modulus H. A schematic showing a point load with a distance r and oriented at an angle of θ from the crack tip is presented in Fig. 16.

The weight function can be calculated as follows:

$$h_x = \frac{H}{2K_1}\left(\frac{\partial u^1}{\partial \theta}\frac{\sin\theta}{r} - \frac{\partial u^1}{\partial r}\cos\theta\right)$$
$$h_y = \frac{H}{2K_1}\left(\frac{\partial v^1}{\partial \theta}\frac{\sin\theta}{r} - \frac{\partial v^1}{\partial r}\cos\theta\right). \tag{19}$$

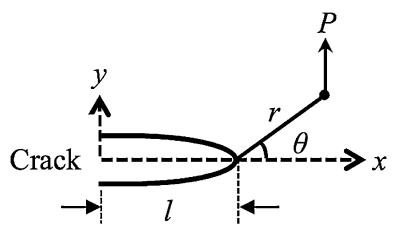

Fig. 16 A schematic showing arbitrary point loading at the crack tip

Appendix 3: 3D Elastic Moduli Representation

The elastic moduli tensor is represented with 3D images in Fig. 5 for Ni_2FeGa. For completeness, we provide the moduli images for the two other alloys, NiTi and CuZnAl (Fig. 17).

Appendix 4: Transformation Strains

The lattice constants of three of the alloys considered result in the following transformation matrix which can be used to establish the transformation strains (Table 8).

The following equation can be used to establish the transformation strains, $\varepsilon = \sqrt{\hat{e}^T F^T F \hat{e}} - 1$ where F is the deformation gradient and is related to the transformation matrix given below by a unique rotation ($F = RU$ and $RR^T = I$), and $\hat{e}$ is any direction in which the transformation strain is calculated.

More detailed explanations can be found in Saburi and Nenno [30], Sehitoglu et al. [34] and in a textbook by Bhattacharya [43]. The volumetric strain can be obtained as $\det(U) - 1$. This volumetric strain was used to estimate the transformation strain in the third dimension when in-plane strains were measured via DIC.

The entire stereographic triangle for the three alloys is given in Fig. 18 showing the maximum transformation strains. We calculated the Ni_2FeGa and CuZnAl transformation strain stereographic triangles in this study while the NiTi stereographic triangle (the detwinning strain version) was published previously [43].

The important observation is that the transformation strains in all shape memory alloys considered are as high as 10 %. We point out that transformation strains were measured for the Ni_2FeGa at the maximum and minimum loads and were used in the calculations. Because we do not have the experimental results of DIC measurements during fatigue crack growth for NiTi and CuZnAl, these strains were assumed to be the same magnitude as Ni_2FeGa. Admittedly, this is a considerable effort that needs to be undertaken in future studies.

Appendix 5: Elastic Moduli Determination

An example of the energy variation as a function of the applied displacement fields is illustrated in Fig. 19 to establish the elastic constants in tetragonal Ni_2FeGa.

In the following analysis, we demonstrate how to calculate the C_{33} for tetragonal Ni_2FeGa. We applied small strain (δ) varying from −0.03 to 0.03 to minimize the errors from higher order terms in the following equation:

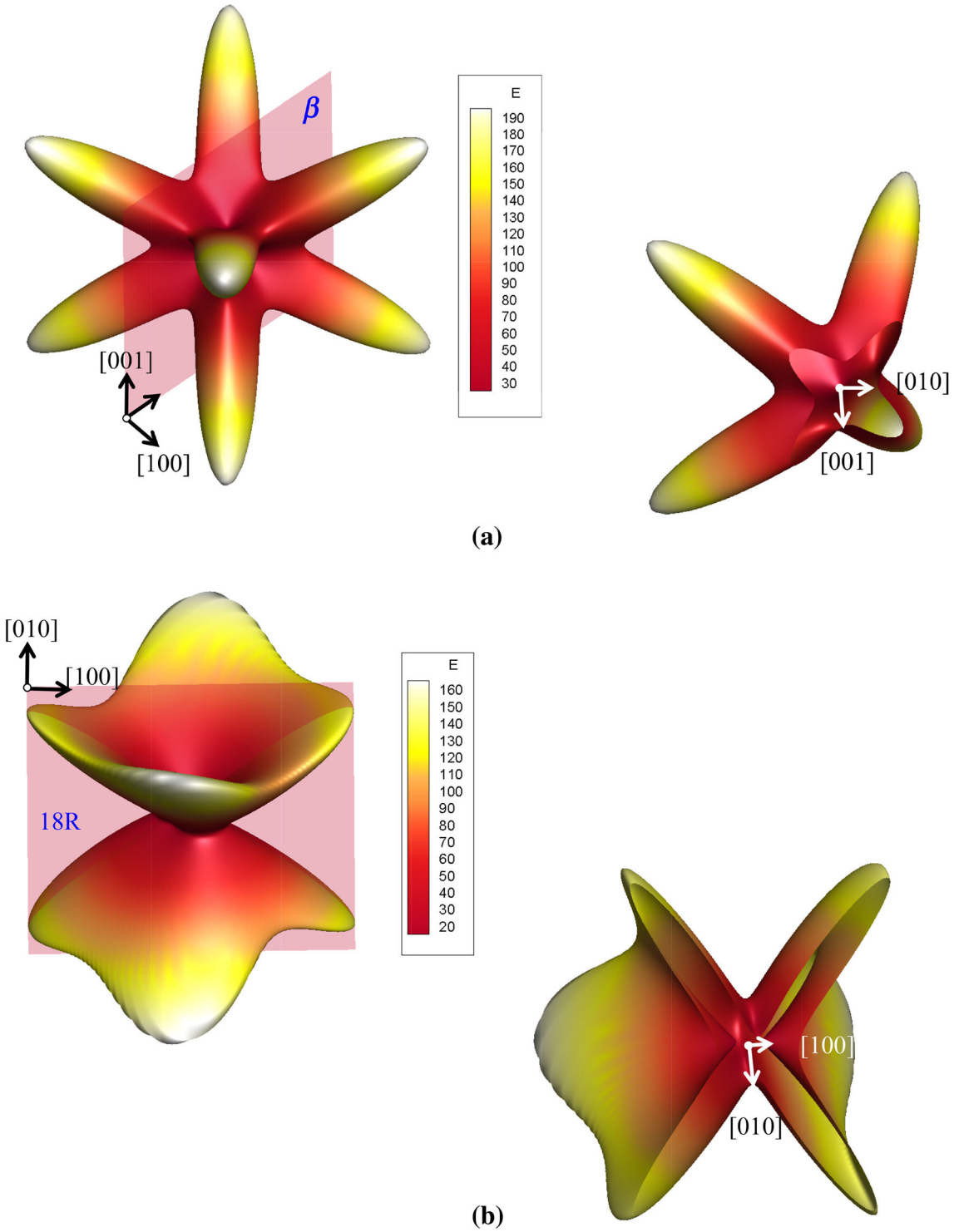

Fig. 17 **a** 3-D representation of austenitic CuZnAl, **b** martensitic CuZnAl, **c** austenitic NiTi, **d** martensitic NiTi

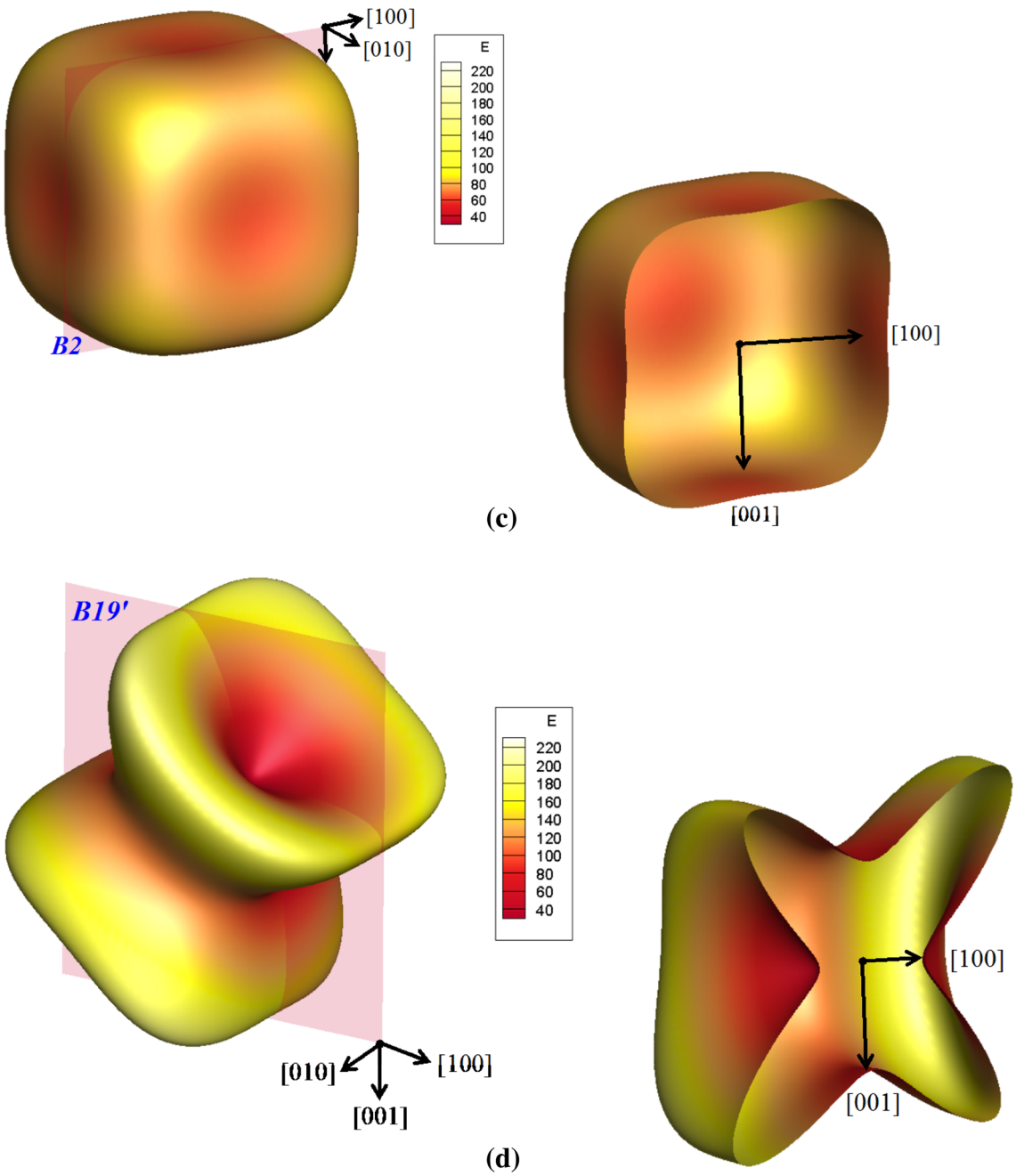

Fig. 17 continued

Table 8 The transformation matrix components for Ni_2FeGa, NiTi, and CuZnAl

Material	U_{11}	U_{22}	U_{33}	U_{12}	U_{13}	U_{23}
Ni_2FeGa	0.9354	0.9354	1.1354	0	0	0
NiTi	0.9563	1.0243	1.0243	−0.0427	−0.0427	0.0580
CuZnAl	1.0101	1.0866	0.9093	0.0249	0	0

$$E(V,\varepsilon) = E(V_o,0) + V_o \sum_{i=1}^{6} \sigma_i \varepsilon_i + \frac{V_o}{2} \sum_{i,j=1}^{6} C_{ij} \varepsilon_i \varepsilon_j + O(\varepsilon^3). \tag{20}$$

The distortion matrix to calculate C_{33} (see Table 2) is given by

$\varepsilon_3 = \delta$

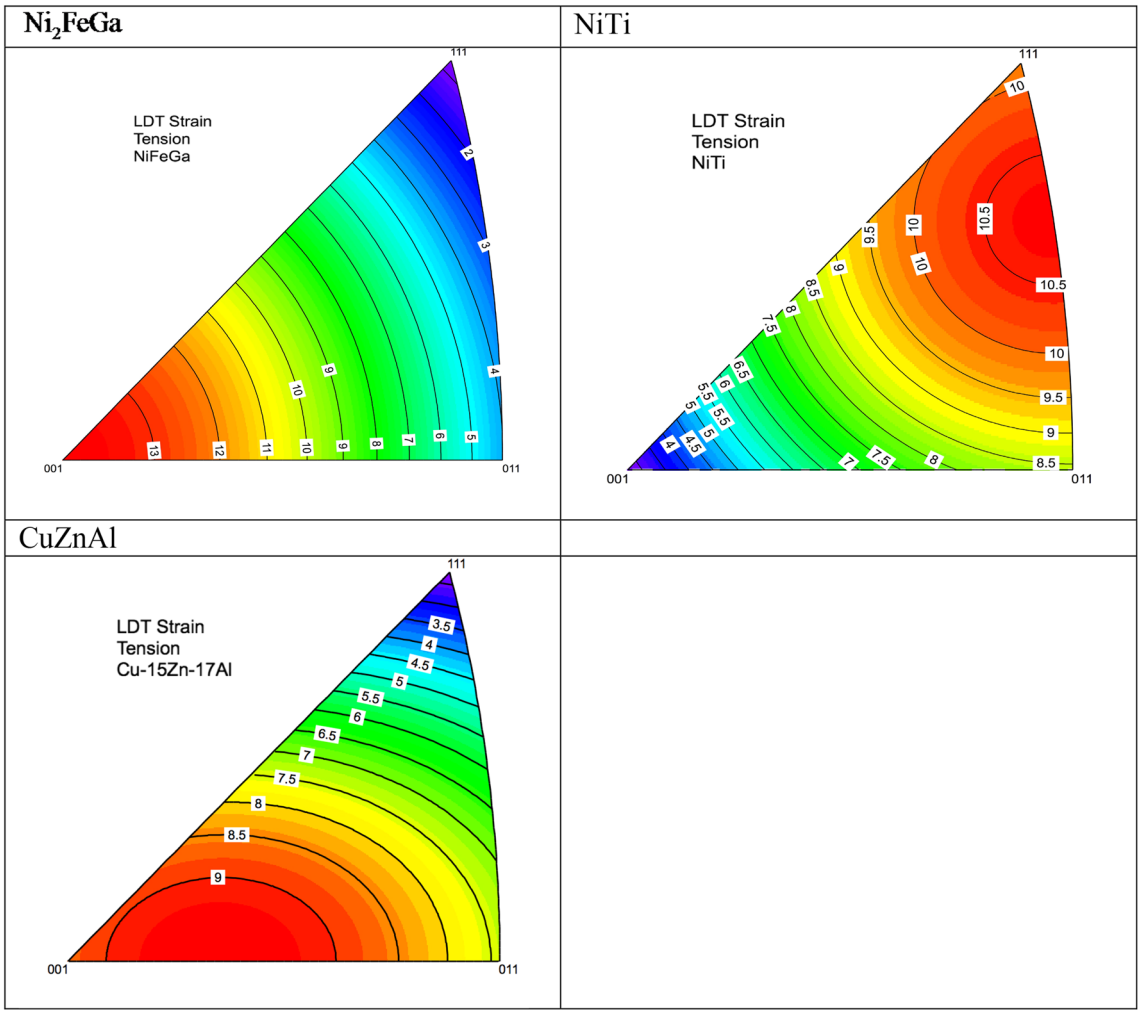

Fig. 18 The transformation strains in tension for Ni_2FeGa, NiTi and CuZnAl considered in this study

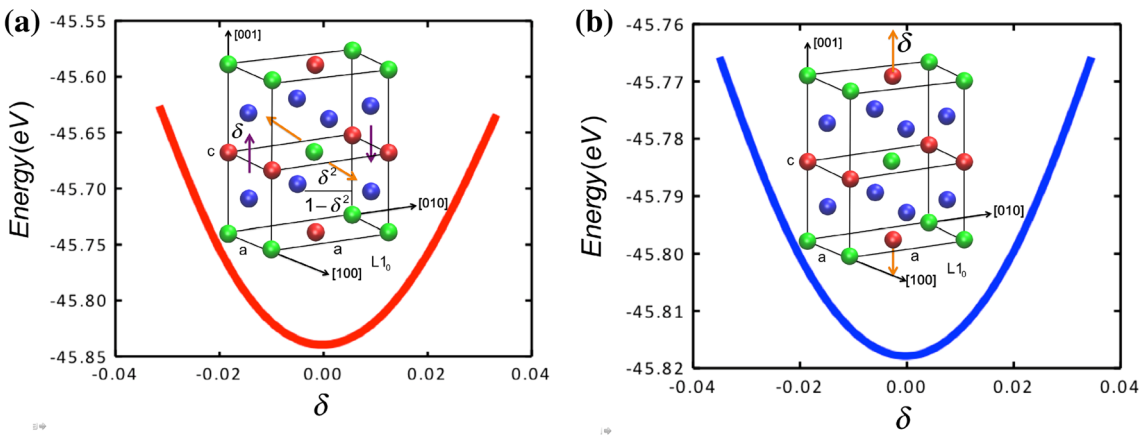

Fig. 19 Energy variation due to infinitesimal distortions in a tetragonal lattice (Ni_2FeGa) **a** for C_{44} calculation, **b** for C_{33} calculation

Therefore, Eq. (20) becomes

$$E(V,\delta) = E(V_o,0) + V_o\left(\sigma_3\delta + \frac{C_{33}}{2}\delta^2\right). \quad (21)$$

We calculate the energy variation of the crystal subjected to different magnitudes of strain and the results are shown in Fig. 19b. The blue curve is a second-order polynomial function to fit these values, and can be written as follows:

$$E(\delta) = 62.87\delta^2 - 0.1006\delta - 45.812. \quad (22)$$

We equate the second-order coefficient of Eq. (22) to the C_{33} elastic constant in Eq. (21) (note that the energy unit is eV, and 1 eV = 1.6×10^{-19} J), and calculate the C_{33} as follows:

$$\left(V_o \times \frac{C_{33}}{2}\right)\delta^2 = \left(62.87 \times 1.6 \times 10^{-19}\right)\delta^2 \quad (23)$$

Substituting the volume of the crystal (V_o) to be 94.69 Å$= 94.69 \times 10^{-30}\,\mathrm{m}^3$ into Eq. (23), we calculate the C_{33} to be 212 GPa. All other elastic constants are calculated following similar procedure.

References

1. Duerig TW, Melton K, Stockel D, Wayman C (1990) Engineering aspects of shape memory alloys. Butterworth-Heinemann, London
2. Otsuka K, Wayman CM (eds) (1998) Shape memory materials. Cambridge University Press, Cambridge
3. McMeeking RM, Evans AG (1982) Mechanics of transformation-toughening in brittle materials. J Am Ceram Soc 65:242–246
4. Rice JR (1972) Some remarks on elastic crack-tip stress fields. Int J Solids Struct 8:751–758. doi:10.1016/0020-7683(72)90040-6
5. Xiong F, Liu Y (2007) Effect of stress-induced martensitic transformation on the crack tip stress-intensity factor in Ni-Mn-Ga shape memory alloy. Acta Mater 55:5621–5629. doi:10.1016/j.actamat.2007.06.031
6. Irwin GR (1960) Plastic zone near a crack and fracture toughness. In: Proceedings of the Sagamore Res Ord Materials Section IV, pp 63–71
7. Baxevanis T, Parrinello AF, Lagoudas DC (2013) On the fracture toughness enhancement due to stress-induced phase transformation in shape memory alloys. Int J Plast 50:158–169. doi:10.1016/j.ijplas.2013.04.007
8. Lexcellent C, Thiebaud F (2008) Determination of the phase transformation zone at a crack tip in a shape memory alloy exhibiting asymmetry between tension and compression. Scripta Mater 59:321–323. doi:10.1016/j.scriptamat.2008.03.040
9. Stam G, van der Giessen E (1995) Effect of reversible phase transformations on crack growth. Mech Mater 21:51–71. doi:10.1016/0167-6636(94)00074-3
10. Brown LC (1979) The fatigue of pseudoelastic single crystals of a-CuAINi. Metall Mater Trans A 10:217–224. doi:10.1007/BF02817631
11. Delaey L, Janssen J, Van de Mosselaer D, Dullenkopf G, Deruyttere A (1978) Fatigue properties of pseudoelastic Cu·Zn·Al alloys. Scripta Metall. 12:373–376. doi:10.1016/0036-9748(78)90302-2
12. Hornbogen E, Eggeler G (2004) Surface aspects in fatigue of shape memory alloys (SMA). Mater. Werkst 35:255–259. doi:10.1002/mawe.200400759
13. Melton KN, Mercier O (1979) Fatigue of NiTi thermoelastic martensites. Acta Metall 27:137–144
14. Miyazaki S, Mizukoshi K, Ueki T, Sakuma T, Liu Y (1999) Fatigue life of Ti–50 at.% Ni and Ti–40Ni–10Cu (at.%) shape memory alloy wires. In: ICOMAT 98. International conference on martensitic transformations, 7–11 Dec. 1998. Elsevier, pp 658–663. doi:10.1016/s0921-5093(99)00344-5
15. Sade M, Hornbogen E (1988) Fatigue of single- and polycrystalline—CuZn-base shape memory alloys. Z Metall 79:782–787
16. Yang NYC, Laird C, Pope DP (1977) The cyclic stress–strain response of polycrystalline, pseudoelastic Cu-14.5 wt pct Al-3 wt pct Ni alloy. Metall Mater Trans A 8:955–962. doi:10.1007/BF02661579
17. McKelvey AL, Ritchie RO (1999) Fatigue-crack propagation in Nitinol, ashape-memory and superelastic endovascular stent material. J Biomed Mater Res 47:301–308
18. McKelvey AL, Ritchie RO (2001) Fatigue-crack growth behavior in the superelastic and shape-memory alloy nitinol. Metall Mater Trans A 32:731–743. doi:10.1007/s11661-001-1008-7
19. Robertson SW, Mehta A, Pelton AR, Ritchie RO (2007) Evolution of crack-tip transformation zones in superelastic nitinol subjected to in situ fatigue: a fracture mechanics and synchrotron X-ray microdiffraction analysis. Acta Mater 55:6198–6207
20. Holtz RL, Sadananda K, Imam MA (1996) Near-threshold fatigue crack growth behavior of nickel-titanium shape memory alloys. In: Johannes Weertman symposium. Proceedings of a symposium held during the TMS annual meeting, 4–8 Feb. 1996, Warrendale, pp 297–299
21. Vaidyanathan R, Dunand DC, Ramamurty U (2000) Fatigue crack-growth in shape-memory NiTi and NiTi–TiC composites. Mater Sci Eng A 289:208–216. doi:10.1016/S0921-5093(00)00882-0
22. Wang J, Sehitoglu H (2014) Martensite modulus dilemma in monoclinic NiTi-theory and experiments. Int J Plast 61:17–31. doi:10.1016/j.ijplas.2014.05.005
23. Hatcher N, Kontsevoi OY, Freeman AJ (2009) Role of elastic and shear stabilities in the martensitic transformation path of NiTi. Phys Rev B 80:144203
24. Wagner MFX, Windl W (2008) Lattice stability, elastic constants and macroscopic moduli of NiTi martensites from first principles. Acta Mater 56:6232
25. Eshelby JD (1957) The determination of the elastic field of an ellipsoidal inclusion, and related problems. Proc R Soc Lond Ser A Math Phys Sci 241:376–396. doi:10.2307/100095
26. Sih GC, Paris PC, Irwin GR (1965) On cracks in rectilinearly anisotropic bodies. Int J Fract Mech 1:189–203. doi:10.1007/BF00186854
27. Efstathiou C, Sehitoglu H, Carroll J, Lambros J, Maier HJ (2008) Full-field strain evolution during intermartensitic transformations in single-crystal NiFeGa. Acta Mater 56:3791–3799. doi:10. 1016/j.actamat.2008.04.033
28. Efstathiou C, Sehitoglu H, Lambros J (2010) Multiscale strain measurements of plastically deforming polycrystalline titanium: role of deformation heterogeneities. Int J Plast 26:93
29. Hamilton ARF, Sehitoglu H, Efstathiou C, Maier HJ (2007) Mechanical response of NiFeGa alloys containing second-phase particles. Scripta Mater 57:497–499
30. Saburi T, Nenno S (1981) The shape memory effect and related phenomena. In: Aaronson HI, Laughlin DE, Sekerka RF, Wayman CM (eds) International conference on solid-solid phase transformations, Pittsburgh, pp 1455–1479

31. Kresse G, Furthmuller J (1996) Efficient iterative schemes for ab initio total-energy calculations using a plane-wave basis set. Phys Rev B 54:11169
32. Rodriguez PL, Lovey FC, Guenin G, Pelegrina JL, Sade M, Morin M (1993) Elastic constants of the monoclinic 18R martensite of a CuZnAl alloy. Acta Metall Mater 41(11):3307–3310
33. Verlinden B, Suzuki T, Delaey L, Guenin G (1984) Third order elastic constants of β Cu-Zn-Al as a function of the temperature. Scripta Metall 18:975–979
34. Ranganathan SI, Ostoja-Starzewski M (2008) Universal elastic-anisotropy index. Phys Rev Lett 101(5):055504
35. Carroll J, Efstathiou C, Lambros J, Sehitoglu H, Hauber B, Spottswood S, Chona R (2009) Investigation of fatigue crack closure using multiscale image correlation experiments. Eng Fract Mech 76(15):2384–2398
36. Pérez-Landazábal JI, Recarte V, Sánchez-Alarcos V, Rodríguez-Velamazán JA, Jiménez-Ruiz M, Link P, Cesari E, Chumlyakov YI (2009) Lattice dynamics and external magnetic-field effects in Ni-Fe-Ga alloys. Phys Rev B 80(14):144301
37. Ren X, Miura N, Zhang J, Otsuka K, Tanaka K, Koiwa M, Suzuki T, Chumlyakov YI, Asai M (2001) A comparative study of elastic constants of Ti-Ni based alloys prior to martensitic transformation. Mater Sci Eng A 312:196–206
38. Mura T (1987) Micromechanics of defects in solids, vol 3. Springer
39. Chowdhury PB, Sehitoglu H, Rateick RG (2014) Predicting fatigue resistance of nano-twinned materials: Part I—role of cyclic slip irreversibility and Peierls stress. Int J Fatigue 68:277–291
40. Chowdhury PB, Sehitoglu H, Rateick RG (2014) Predicting fatigue resistance of nano-twinned materials: Part II—effective threshold stress intensity factor range. Int J Fatigue 68:292–301
41. Sehitoglu H, Wang J, Maier HJ (2012) Transformation and slip behavior of Ni_2FeGa. Int J Plast 39:61–74
42. Sehitoglu H, Zhang XY, Chumlyakov YI, Karaman I, Gall K, Maier HJ (2002) Observations on stress-induced transformations in NiTi alloys. In: IUTAM symposium on mechanics of martensitic phase transformation in solids. Springer, New York, pp 103–109
43. Sehitoglu H, Karaman I, Anderson R, Zhang X, Gall K, Maier HJ, Chumlyakov Y (2000) Compressive response of NiTi single crystals. Acta Mater 48(13):3311–3326